

# The GHOSDT Simulations (Galaxy Hydrodynamical Simulations with Supernova-Driven Turbulence) - I. Magnetic Support in Gas Rich Disks

ALON GURMAN,<sup>1</sup> ULRICH P. STEINWANDEL,<sup>2</sup> CHIA-YU HU (胡家瑜),<sup>3,4</sup> AND AMIEL STERNBERG<sup>1,2,5</sup>

<sup>1</sup>*School of Physics & Astronomy, Tel Aviv University, Ramat Aviv 69978, Israel*

<sup>2</sup>*Center for Computational Astrophysics, Flatiron Institute, 162 5th Ave, New York, NY 10010, USA*

<sup>3</sup>*Department of Astronomy, University of Florida, 211 Bryant Space Sciences Center, Gainesville, FL 32611 USA*

<sup>4</sup>*Institute of Astrophysics and Department of Physics, National Taiwan University, No. 1, Sec. 4, Roosevelt Rd., Taipei 10617, Taiwan*

<sup>5</sup>*Max-Planck-Institut für Extraterrestrische Physik, Giessenbachstrasse 1, D-85748 Garching, Germany*

## ABSTRACT

Galaxies at redshift  $z \sim 1-2$  display high star formation rates (SFRs) with elevated cold gas fractions and column densities. Simulating a self-regulated ISM in a hydrodynamical, self-consistent context, has proven challenging due to strong outflows triggered by supernova (SN) feedback. At sufficiently high gas column densities, and in the absence of magnetic fields, these outflows prevent a quasi-steady disk from forming at all. To this end, we present GHOSDT, a suite of magneto-hydrodynamical simulations that implement ISM physics at high resolution. We demonstrate the importance of magnetic pressure in the stabilization of gas-rich star-forming disks. We show that a relation between the magnetic field and gas surface density emerges naturally from our simulations. We argue that the magnetic field in the dense, star-forming gas, may be set by the SN-driven turbulent gas motions. When compared to pure hydrodynamical runs, we find that the inclusion of magnetic fields increases the cold gas fraction and reduces the disc scale height, both by up to a factor of  $\sim 2$ , and reduces the star formation burstiness. In dense ( $n > 100 \text{ cm}^{-3}$ ) gas, we find steady-state magnetic field strengths of 10–40  $\mu\text{G}$ , comparable to those observed in molecular clouds. Finally, we demonstrate that our simulation framework is consistent with the Ostriker & Kim (2022) Pressure Regulated Feedback Modulated Theory of star formation and stellar Feedback.

*Keywords:* Interstellar medium (847) – Hydrodynamical Simulations (767)

## 1. INTRODUCTION

Stars form in cold, dense, molecular clouds (McKee & Ostriker 2007). Static models of the multiphase interstellar medium (ISM) capture the relationship between the ISM and star formation, in which the phase distribution and gas conditions of the ISM are affected by energy injection from stars in the form of radiative- and supernova feedback (Klessen & Glover 2016; Naab & Ostriker 2017). The time-dependent picture, however, is more complex, as dynamical processes such as the cycle of cooling, gravitational collapse, and subsequent radiative, shock heating, and dispersal of clouds, take place rapidly and are affected by the large-scale gravitational

potential, gas weight, and star-formation-rate (SFR), to name a few (e.g., Ostriker & Shetty 2011; Hu et al. 2021; Ostriker & Kim 2022). As such, dynamical models of the ISM in the form of 3D (magneto-)hydrodynamical simulations on different scales have been devised and implemented at high resolution on different physical scales. Stratified box setups, also referred to as galactic patches, strike a balance between simulation volume, spatial resolution, and simulation time. They combine (sub-)pc resolution with a kpc-scale box size, and several 100 Myr of simulation time, and, as such, provide several benefits (see, e.g., de Avillez & Breitschwerdt 2004; Joung & Mac Low 2006; Hill et al. 2012; Hennebelle & Iffrig 2014; Walch et al. 2015; Girichidis et al. 2015; Kim & Ostriker 2015; Simpson et al. 2016; Hu et al. 2016, 2017; Kim & Ostriker 2018; Kim et al. 2020a,b; Kannan et al. 2020; Hu et al. 2021; Brucy et al. 2023a; Rathjen et al.

2023; Kim et al. 2024; Rathjen et al. 2024). This treatment allows for the (potential) resolution of the dense, clumpy, molecular cores of star-forming clouds, with a large enough volume for capturing gas compression on the scale of several 100 pc by SN shocks. The long simulation time means that several life cycles of molecular clouds can be captured, and their stochastic nature is properly sampled. In addition, it allows averaging large fluctuations of different ISM properties over time. Finally, at this scale, star formation can be tracked on a star-by-star level, meaning that stars are formed individually, and their associated feedback can be treated without the need for stellar population synthesis models. Other high-resolution simulations of galactic patches (e.g., Kim & Ostriker 2017; Walch et al. 2015) form star clusters rather than single stars, by setting conditions for the formation of sink particles that are then allowed to accrete gas from their environment. SN and photoionization feedback are then computed based on the accretion history of the sink particles. Additionally, while there are clear advantages to tracking individual star formation, we do not account for the evolution of stellar winds, which could impact the structure and extent of photoionized regions before SN feedback disrupts them entirely (Haid et al. 2018; Lancaster et al. 2021a,b; Grudić et al. 2021, 2022).

Our star formation and feedback prescription was first introduced in Hu et al. (2016), and subsequently developed in Hu et al. (2017) in the SPH code GADGET, which was then applied to simulations of multiphase galactic winds (Hu 2019), and adopted as the default feedback model in the GRIFFIN simulations (Lahén et al. 2020b) of a dwarf galaxy merger. Since then, it has undergone further modifications, including the switch to the meshless finite mass method (MFM) in the GADGET code by Steinwandel et al. (2020). The MFM version of the code has subsequently been applied to isolated dwarf galaxy simulations that probe the effects of runaway stars (Steinwandel et al. 2023), the variability of the SN-feedback energy (Steinwandel & Goldberg 2023), has further pushed the development version of the code to more massive systems such as the LMC (Steinwandel et al. 2024a) and has introduced the importance of metal diffusion models for the metal phase structure in the ISM and multiphase galactic outflows (Steinwandel et al. 2024b). The SPH version of this code has been further applied to investigate the formation and evolution of star clusters (Hislop et al. 2022; Lahén et al. 2019, 2020b,a, 2023, 2024), as well as molecular clouds (Fotopoulos et al. 2024), in part, by adopting a fully

sampled IMF and the enrichment by stellar winds of supermassive stars in dwarf galaxy systems, as well as accretion onto black holes (Partmann et al. 2024). This feedback model was then implemented into the GIZMO code and applied in stratified box simulations (Hu et al. 2021), isolated dwarf galaxy simulations for a code comparison paper (Hu et al. 2023b), and improved dust modelling (Hu et al. 2023a). These efforts have inspired the further application of similar techniques to other multi-purpose astrophysical codes such as ENZO (Emerick et al. 2019, 2020a,b), AREPO (Smith 2021; Gutcke et al. 2021, 2022a,b; Deng et al. 2024), RAMSES (Andersson et al. 2020, 2023, 2024; Calura et al. 2022) and ASURA+BRIDGE (Hirai et al. 2021; Fujii et al. 2021a,b, 2022b,a, 2024). In the following we will only summarize the work in stratified box simulations in greater detail as these are the most important simulations in comparison to our work.

Hu et al. (2021, hereafter HSvD21) performed a suite of hydrodynamical simulations of a  $(1 \times 1 \times 10)$  kpc<sup>3</sup> ISM patch. Incorporating a particle resolution of  $1 M_{\odot}$  ( $\sim 0.2$  pc), a 500 Myr simulation time, and 4 different metallicities ranging from  $Z/Z_{\odot} = 0.1$  to 3, and including a star-by-star treatment of star formation and SN feedback, their setup was optimal for investigating the properties of the cold (molecular) ISM. Comparing a steady-state and a time-dependent treatment of hydrogen chemistry, they found that assuming chemical steady state overproduces H<sub>2</sub>, and that this effect is stronger at low metallicity, where the H<sub>2</sub> formation timescale is longer. By using full line radiative transfer, Hu et al. (2022) found that this effect leads to a substantial correction to the widely assumed metallicity dependence of the CO-to-H<sub>2</sub> conversion factor,  $X_{\text{CO}}$ , and Gurman et al. (2024) found a linear metallicity dependence in the [CII]–SFR relation, with [CII] emission dominated by high-density gas.

On average, galaxies at  $z \sim 1 - 2$ , form stars at higher rates per stellar mass compared to those at  $z \sim 0$  (Madau & Dickinson 2014), with Milky Way mass galaxies peaking near  $z \sim 1$  (Moster et al. 2018). The cosmic peak of star-formation at  $z \sim 1 - 2$  is associated with larger cold gas fractions and disk gas column densities compared to  $z = 0$  (Tacconi et al. 2020). Galactic patch simulations predict strong SN-driven gas outflows at gas surface densities higher than the solar neighborhood value of the  $\sim 10 M_{\odot} \text{ pc}^{-2}$ . The increase in outflows is in direct correlation to the gas surface density, which, in turn, causes an increase in SFR as is observed in the Kennicutt-Schmidt relation on both ISM and

galaxy-integrated scales (Kennicutt 1998; Bigiel et al. 2008). In simulations, these strong outflows can potentially disrupt the emerging gaseous disks entirely, making them challenging to simulate. Successful simulations at this scale with high gas-surface densities have been presented by Kim et al. (2020a); Rathjen et al. (2023); Bruzy et al. (2023a). In all of the above, a combination of magnetic fields and (temporary) artificial turbulent driving have been implemented to moderate the large-scale, simultaneous, vertical collapse of the disk, and the subsequent intense SN-driven outflows. This enables the retention of much of the gas in the box for a longer period and hence successful simulations. In the absence of the aforementioned precautions, as in the setup of HSvD21, these simulations are known to blow out most of their gas, while the remaining gas fails to settle into a star-forming disk, and the star formation rate falls well below the observed Kennicutt-Schmidt relation.

The effects of magnetic fields in a self-regulated ISM have been studied at solar neighborhood conditions, i.e.,  $\Sigma_{\text{gas}} \approx 10 M_{\odot} \text{ pc}^{-2}$ . Hill et al. (2012) compared the ISM phase structure in pure hydrodynamical simulations to that of magnetohydrodynamical (MHD) simulations with different initial magnetic fields. They found that the cold gas mass fractions are lower for the MHD runs, likely due to magnetic support against the vertical compressions of their initial disk setups. However, they did not include self-gravity, temporal and spatial variations in the FUV radiation field, or a self-consistent positioning of the SN explosions. Hennebelle & Iffrig (2014) include self-gravity in their simulations, and position an SN explosion in the vicinity of stellar sink particles whenever they accrete  $120 M_{\odot}$ . While their simulation time of  $\lesssim 100$  Myr is rather short, they find that their hydrodynamical run forms stars in shorter, more intense bursts, compared to the MHD runs, while the total mass in stars formed is reduced slightly by the inclusion of magnetic fields, as long as the initial field is strong enough. Using a similar setup Iffrig & Hennebelle (2017) explored higher initial magnetic field strengths. They found a reduction of up to an order of magnitude in the SFR for the MHD simulations compared to pure hydrodynamical simulations. The simulation time of  $\lesssim 100$  Myr limited their study to the initial burst of star formation following the vertical collapse of their initial disk setup. They also found that the orientation of the magnetic field, initially set to be uniform and in the disk plane, mostly retained its initial direction even at the end of their simulations, indicating the persistence of the initial magnetic field configuration. In a compar-

ison between hydrodynamical and MHD ISM patches with different initial magnetic field strengths and configurations, Kim & Ostriker (2015) found that stronger magnetic fields reduce the scale height of the disk as well as the SFR. They note that in their strongest magnetic field runs, the magnetic field strength does not reach steady state, and was still dominated by the value set by the initial conditions, even at late times. Girichidis et al. (2018) found that including magnetic fields leads to a larger disk scale height, but this is likely due to their simulation time ( $\sim 60$  Myr) being limited to the collapse of their initial disk setup. As such, magnetic support simply slows down the vertical collapse and creates an effectively thicker disk. This effect also explains why their MHD runs show a delayed onset of  $\text{H}_2$  and star formation, as both are correlated with the compression of the disk. They also found that the relationship between gas density and magnetic field strength is almost unaffected by a factor of two change in the initial magnetic field. Gressel et al. (2008) simulated a SN-regulated ISM with resistive MHD and a spatially constant magnetic diffusivity. They compared models with Cartesian shear to models with differential rotation, and found that while both displayed an amplification of the root mean square magnetic field, the mean magnetic field could only be amplified when differential rotation was included. Bruzy et al. (2023b) find that for high gas surface density, increasing the magnetic field can reduce the SFR by 2-3 orders of magnitude. It should be noted that due to the bursty star formation in their gas-rich models, they restricted their analysis in these cases to the first, strong burst of star formation. Since this is the first event of star formation, the gas has yet to experience regulation by SNe, and thus the SFR could become rather sensitive to initial conditions.

In this work, we present GHOSDT (Galaxy Hydrodynamical Simulations with Supernova-Driven Turbulence), a suite of high-resolution, magnetohydrodynamical ISM simulations, spanning gas surface densities in the range of  $4\text{-}100 M_{\odot} \text{ pc}^{-2}$ . In Sec. 2, we describe our numerical setup and different simulation runs. In Sec. 3, we present an overview of the simulation results and the effect of magnetic fields. In Sec. 4, we investigate the dependence of the magnetic field on the gas surface density and initial conditions. In Sec. 5, we summarize our results and discuss future prospects for the simulations.

## 2. NUMERICAL METHODS

GHOSDT builds on the simulations of [HSvD21](#), and follows the same implementation of cooling, heating, chemistry, star formation, and stellar feedback. We extend their setup by including magnetic fields and varying the initial gas surface density in order to study the higher column density regime.

### 2.1. Gravity and MHD

We employ the publicly available version of GIZMO ([Hopkins 2015](#)), a multi-method code implementing the meshless Godunov-type method ([Gaburov & Nitadori 2011](#)) on top of the TreeSPH code GADGET-3 ([Springel 2005](#)). The gravitational interaction is solved by the “treecode” method outlined in [Barnes & Hut \(1986\)](#), while hydrodynamics are solved by the MFM method ([Hopkins 2015](#)) with the (average) number of neighboring particles in a kernel  $N_{\text{ngb}} = 32$ .

We extend the work of [HSvD21](#) by also including MHD using the GIZMO module introduced by [Hopkins & Raives \(2016\)](#), solving the (ideal) MHD equations, while ensuring numerical stability and maintaining  $\nabla \cdot \mathbf{B} \approx 0$ . This is done using a combination of the Powell 8-wave cleaning ([Powell et al. 1999](#)) and the hyperbolic/parabolic divergence cleaning scheme of [Dedner et al. \(2002\)](#), which we briefly introduce below.

The homogeneous ideal MHD Euler equations for a moving frame with velocity  $\mathbf{v}_{\text{frame}}$  are given by

$$\frac{\partial \mathbf{U}}{\partial t} + \nabla \cdot (\mathbf{F} - \mathbf{v}_{\text{frame}} \otimes \mathbf{U}) = \mathbf{S} \quad (1)$$

where  $\mathbf{U}$  is the vector of conserved variables (in the source-free case),  $\mathbf{F}$  is the tensor consisting of the different fluxes of each conserved variable, and  $\mathbf{S}$  is the source term vector.

$$\mathbf{U} = \begin{pmatrix} \rho \\ \rho \mathbf{v} \\ \rho e \\ \mathbf{B} \\ \rho \psi \end{pmatrix}; \quad \mathbf{F} = \begin{pmatrix} \rho \mathbf{v} \\ \rho \mathbf{v} \otimes \mathbf{v} + P_T \mathcal{I} - \mathbf{B} \otimes \mathbf{B} \\ (\rho e + P_T) \mathbf{v} - (\mathbf{v} \cdot \mathbf{B}) \mathbf{B} \\ \mathbf{v} \otimes \mathbf{B} - \mathbf{B} \otimes \mathbf{v} \\ \rho \psi \mathbf{v} \end{pmatrix} \quad (2)$$

where  $\rho$  is the mass density,  $e = u + |\mathbf{B}|^2/2\rho + |\mathbf{v}|^2/2$  is the total specific energy,  $u$  is the internal energy,  $P_T = P + |\mathbf{B}|^2/2$  is the sum of the thermal and magnetic pressures, and  $\psi$  is a conservative scalar field devised to transport  $\nabla \cdot \mathbf{B}$  away from the source and to damp it, following the method of [Dedner et al. \(2002\)](#).

The discrete meshless evolution equations, fully derived in [Hopkins \(2015\)](#), are then given by

$$\frac{d}{dt} (V \mathbf{U})_i + \sum_j \tilde{\mathbf{F}}_{i,j} \cdot \mathbf{A}_{ij} = (V \mathbf{S})_i. \quad (3)$$

Here,  $(V \mathbf{U})_i$  is the cell-volume integrated valued of conserved quantities to be carried with particle  $i$ , and its rate of change is given by the sum of fluxes  $\tilde{\mathbf{F}}$  into/out of its effective face area  $\mathbf{A}_{ij}$  and the cell-integrated source term  $(V \mathbf{S})_i$ . The full derivation of  $\mathbf{A}_{ij}$  is presented in [Hopkins \(2015\)](#).

The cleaning method described in [Hopkins & Raives \(2016\)](#) adds two source terms,

$$\mathbf{S} = \mathbf{S}_{\text{Powell}} + \mathbf{S}_{\text{Dedner}}, \quad (4)$$

$$= -\nabla \cdot \mathbf{B} \begin{pmatrix} 0 \\ \mathbf{B} \\ \mathbf{v} \cdot \mathbf{B} \\ \mathbf{v} \\ 0 \end{pmatrix} - \begin{pmatrix} 0 \\ 0 \\ \mathbf{B} \cdot (\nabla \psi) \\ \nabla \psi \\ (\nabla \cdot \mathbf{B}) \rho c_h^2 + \rho \psi / \tau \end{pmatrix}.$$

$\mathbf{S}_{\text{Powell}}$  represents the [Powell et al. \(1999\)](#) cleaning, which subtracts the numerically unstable terms resulting from a non-zero  $\nabla \cdot \mathbf{B}$ .  $\mathbf{S}_{\text{Dedner}}$  is the source term formulated in [Dedner et al. \(2002\)](#), where a scalar field  $\psi$  is introduced in order to transport away and damp the non-zero divergence. There is freedom to choose  $c_h$  and  $\tau$  for each particle. For each particle, we use  $c_h = \sigma_h^{1/2} v_{\text{sig}}^{\text{MAX}}/2$  (following [Hopkins & Raives \(2016\)](#); [Tricco & Price \(2012\)](#)), where  $v_{\text{sig}}^{\text{MAX}}$  is the local maximum signal velocity, and  $\sigma_h$  is a dimensionless scaling parameter taken to be 1. We use  $\tau = h/(\sigma_p c_\tau)$ , where  $h$  is the local effective cell height,  $\sigma_p = 0.1$ , and the damping speed  $c_\tau$  is defined in Appendix D of [Hopkins & Raives \(2016\)](#), where the choices of definitions for the above quantities is explored in depth.

### 2.2. ISM Physics and Star Formation

Our treatment of cooling, chemistry, star formation, and feedback, uses the setup presented in [HSvD21](#). Chemistry and cooling are based on [Glover & Mac Low \(2007\)](#) and [Glover & Clark \(2012\)](#) and include time-dependent treatment of hydrogen chemistry, assuming steady state coupling of additional species, e.g.,  $\text{C}^+$ , C, and CO, whose abundances are computed in post-processing, using ASTROCHEMISTRY.JL <sup>1</sup> ([Hu 2021](#)). This is combined with a HEALPIX ([Górski & Hivon 2011](#)) method for the calculation of radiation shielding, which captures  $\text{H}_2$  and dust FUV shielding by determining an effective shielding column density for each particle.

<sup>1</sup> Code is publicly available at <https://github.com/huchiayu/AstroChemistry.jl>

Star formation is implemented using a stochastic recipe. Once the local thermal jeans mass becomes unresolved, i.e., lower than the local kernel mass, a gas particle is assigned a probability of  $\epsilon_{\text{sf}}\Delta t/t_{\text{ff}}$  to be converted into a star particle, where  $\Delta t$  is the time step,  $t_{\text{ff}}$  is the local freefall time, and  $\epsilon_{\text{sf}}$  is the star formation efficiency, assumed to be equal to 0.5, as we resolve the clumpy sub-structure of molecular clouds. The mass of the star is sampled from the IMF (Kroupa 2002), and this determines its photoionizing budget and whether it produces SN feedback.

If a star has mass  $> 8M_{\odot}$ , we use the method presented in Hu et al. (2017), where a spherical ionization front within which hydrogen is assumed to be fully ionized, and the gas is heated to  $\sim 10^4$  K, is computed iteratively until a balance between the (initial mass-dependent) ionizing stellar radiation and the surrounding gas is obtained. Massive stars also inject  $10^{51}$  ergs of thermal energy into their neighbouring particles at the end of their lifetime, which is determined by their initial mass as well. As we resolve the Sedov-Taylor phase of the SN remnant expansion, our SN feedback recipe is insensitive to the form of SN energy injection (Hu 2019).

### 2.3. Simulation Setup

Our simulation setup consists of a spatial domain extending 1 kpc in the  $x$ - and  $y$ -directions, and 50 kpc in the  $z$ -direction. Boundary conditions are periodic in  $x$  and  $y$ , and the  $z$ -dimension has outflow boundary conditions. The mid-plane of the disk is set at  $z = 0$ . In our fiducial initial conditions, the gas initially follows a Spitzer (1942) vertical distribution of the form

$$\rho(z) = \Sigma_{\text{gas},0}/(2H_g) \text{sech}^2(z/H_g) \quad . \quad (5)$$

Here  $\Sigma_{\text{gas},0}$ , the initial total gas surface density, is the main free parameter in this work. We consider the range 4 to  $100 M_{\odot} \text{pc}^{-2}$ . In Eq. (5),  $\rho$  is the gas density, and  $H_g$  is the initial scale height of the disk that we set to 250 pc. At any height  $z$ , the initial acceleration due to self-gravity is

$$a_g = -2\pi G \Sigma_{\text{gas},0} \tanh\left(\frac{z}{H_g}\right) \quad . \quad (6)$$

We also include an external gravitational potential due to a stellar disk and dark matter halo. The contribution to the gravitational acceleration from the stellar disk is

$$a_* = -2\pi G \Sigma_* \tanh\left(\frac{z}{H_*}\right) \quad , \quad (7)$$

where  $\Sigma_* = 40 M_{\odot} \text{pc}^{-2}$  and  $H_* = 250$  pc are typical values at the Galactic solar circle. The dark matter

contribution is derived from an Navarro-Frenk-White profile (NFW; Navarro et al. 1997) with a virial mass  $M_{\text{vir}} = 10^{12} M_{\odot}$  and concentration  $c = 12$ , resulting in

$$a_{\text{DM}} = -\frac{Gm(r)z}{r^3}, \quad (8)$$

where  $r = \sqrt{z^2 + R_0^2}$  is the radial distance from the center of the halo. The enclosed mass  $m(r)$  is given by

$$m(r) = 4\pi r_s^3 \rho_s \ln[(1 + r/r_s) - (r/r_s)(1 + r/r_s)], \quad (9)$$

where  $r_s = 17$  kpc,  $\rho_s = 9.5 \times 10^{-3} M_{\odot} \text{pc}^{-3}$ , and  $R_0 = 8$  kpc is the galactocentric distance to the sun. We keep both  $a_*$  and  $a_{\text{DM}}$  fixed across all of our simulations, independent of the assumed gas surface density.

Our mass resolution is  $m_g = 1 M_{\odot}$  for our high-resolution models and  $m_g = 10 M_{\odot}$  for our low-resolution models. At this resolution, the Sedov-Taylor phase of a SN remnant expansion is captured accurately (Steinwandel et al. 2020). While high resolution is desirable for the correct treatment of SN feedback and resolving the structure of molecular clouds, the computational demands of such high resolution become very high for  $\Sigma_{\text{gas},0} > 40 M_{\odot} \text{pc}^{-2}$ , and we are forced to use lower resolution for those models, setting the gas particle mass to  $10 M_{\odot}$ . For consistency, we run low-resolution models for  $\Sigma_{\text{gas},0} \leq 40 M_{\odot} \text{pc}^{-2}$  as well. This corresponds to an effective spatial resolution of  $\approx 0.2$  pc for our  $1 M_{\odot}$  runs, or  $\approx 0.4$  pc for our  $10 M_{\odot}$  runs. We run our models for 0.5-1 Gyr. Our long simulation times allow us to fully sample the fluctuations in star formation and ISM conditions, as well as the evolution of gas mass and magnetic fields over time.

Only a small number of groups have carried out galactic patch simulations at high resolution with a multi-channel stellar feedback with MHD and high gas surface density models that are evolved past the initial burst of star formation that is common in these systems (e.g., Kim et al. 2020a). Also, our simulations include pure hydrodynamical models up to  $\Sigma_{\text{gas},0} = 80 M_{\odot} \text{pc}^{-2}$ , allowing us to investigate the importance of magnetic fields in these environments.

The initial gas temperature is set to  $10^4$  K everywhere. We adopt a constant solar chemical composition, i.e., carbon and oxygen abundance of  $1.4 \times 10^{-4}$  and  $3.2 \times 10^{-4}$ , respectively (Cardelli et al. 1996; Sembach et al. 2000), and a dust-to-gas mass ratio of 1%.

In our fiducial MHD runs, the magnetic field is set to an initial value  $B_0 \hat{x}$  (parallel to the disk mid-plane), which is constant everywhere. We choose the value of

$B_0$  by attempting to find a value that fulfills the following requirements. First, it should allow for the establishment of a quasi-steady disk, which becomes increasingly important as  $\Sigma_{\text{gas},0}$  increases (see Sec. 3.1). Second, we require that the mass-weighted mean magnetic field in the dense ( $n > 100 \text{ cm}^{-3}$ ) gas reaches a quasi-steady value. Since the magnetic field strength varies in time following fluctuations in SFR, we first apply a moving average with a 200 Myr window, and then visually check for convergence. Third, we require that the absolute value of the  $x$ - and  $y$ -components of the magnetic become comparable. We do so by requiring that the mass-weighted average of  $(\mathbf{B}_x/|\mathbf{B}|)^2$  decreases to a value close to 1/3, roughly indicating equipartition of the different magnetic field components. We show that this holds for our simulations in Sec. 4 and Appendix B. Finally, we check that the mean magnetic field is negligible compared to the root mean square magnetic field. Under these conditions, the simulation results are quite insensitive to the value of  $B_0$ , even when it is varied by orders of magnitude.

#### 2.4. Simulation List

Our simulation runs are labeled and listed in Tab. 1. Simulation groups H and M use our stratified disk initial conditions described in Sec. 2.3 with different values of  $\Sigma_{\text{gas},0}$ . Simulations in group H are run with magnetic fields switched off, while simulations in group M include magnetic fields whose initial  $x$ -component is set to  $B_0$ . Simulations in groups HV and MV are run with magnetic fields turned off and on, respectively, but with initial conditions that differ from groups H and M. Instead of a stratified disk, the initial conditions for groups with added label V are set using the outputs from the simulations of group M at 200 Myr, with the corresponding value of  $\Sigma_{\text{gas},0}$ . Then, in group HV, the simulation is restarted with magnetic fields turned off. In group MV, each directional component of the initial magnetic field at each particle is set by drawing from a Gaussian random distribution with a standard deviation equal to  $B_0$ . While these initial conditions are not designed to satisfy the condition  $\nabla \cdot \mathbf{B} = 0$ , the employed divergence cleaning scheme ensures that  $\nabla \cdot \mathbf{B}$  becomes comparable to that of our fiducial runs within  $\sim 10$  Myr. The aim of groups HV and MV is to use initial conditions that are well mixed and less symmetrical, compared with the setup in groups H and M.

When referring to a single simulation, we specify the value of  $\Sigma_{\text{gas},0}$  in units of  $M_\odot \text{ pc}^{-2}$  following the group name (e.g., M20 belongs to group M and has  $\Sigma_{\text{gas},0}$

set to  $20 M_\odot \text{ pc}^{-2}$ ). In addition, we supplement the simulations in Tab. 1 with an additional set of simulations whose purpose is to verify the insensitivity of the emerging magnetic field to our initial conditions. These simulations are listed and discussed in Sec. 4. Unless explicitly stated otherwise, we only analyze our simulation data at times later than 200 Myr, to mitigate the effects of our initial conditions. This timescale is a combination of the initial free-fall and cooling times of the initial disk, followed by strong outflows, and then a second round of inflows, after which the disk can establish itself. This timescale also changes for different simulations, with the low  $\Sigma_{\text{gas},0}$  runs generally taking longer for the initial collapse. 200 Myr is generally long enough to capture this period across all of our different simulations. Simulations that were run for a much shorter time period, like some existing works in the literature, would be significantly affected by the initial conditions.

### 3. RESULTS

#### 3.1. Star Formation Rate

Fig. 1 shows the average Kennicutt-Schmidt (KS) relation between the SFR surface density  $\Sigma_{\text{SFR}}$  ( $M_\odot \text{ yr}^{-1} \text{ kpc}^{-2}$ ) and the gas surface density  $\Sigma_{\text{gas}}$  ( $M_\odot \text{ pc}^{-2}$ ), for our simulation groups H, M, and HV. For each snapshot, we set

$$\text{SFR} = \frac{M_*( < t_{\text{SFR}})}{t_{\text{SFR}}}, \quad (10)$$

where  $M_*( < t_{\text{SFR}})$  is the mass in stars with ages less than an adopted star-formation timescale  $t_{\text{SFR}} = 10$  Myr. We further divide the SFR by our box surface area of  $1 \text{ kpc}^2$  to obtain  $\Sigma_{\text{SFR}}$ . Because the gas surface density decreases with time as gas is driven out of the box boundaries by SN feedback, especially for  $\Sigma_{\text{gas},0} \geq 40 M_\odot \text{ pc}^{-2}$ , for each group we bin individual snapshots taken at time intervals of 1 Myr according to their gas surface density. Next, we compute the medians and means of  $\Sigma_{\text{SFR}}$  for the snapshots in each bin. Results are presented in the top and bottom panels of Fig. 1, respectively. We also plot power laws of the form  $\Sigma_{\text{SFR}} \propto \Sigma_{\text{gas}}^N$  for  $N = (1.4, 1.7, 2)$ , the observed solar neighborhood value from Fuchs et al. (2009), and results from the TIGRESS simulation R-models (Kim et al. 2020a), group TURB from Bruzy et al. (2023a), and the SILCC project (Rathjen et al. 2023).

We find that our different simulation groups agree in their KS relations to within a factor of  $\sim 2$ , except group H which shows a decrease in  $\Sigma_{\text{SFR}}$  for  $\Sigma_{\text{gas}} \gtrsim 40 M_\odot \text{ pc}^{-2}$ . These small differences do not seem systematic and occur even within a single model by stop-

Name	$\Sigma_{\text{gas}} (M_{\odot} \text{ pc}^{-2})$	$B_0 (\mu\text{G})$	$M_{\text{gas}} (M_{\odot})$	$t_{\text{sim}} (\text{Gyr})$
H4, H10, H20	4, 10, 20	N/A	1 (10)	0.5 (1)
H40, H60, H80	40, 60, 80	N/A	10	0.5
M4	4	0.05	1 (10)	1
M10	10	0.05	1 (10)	0.5 (1)
M20	20	2	1 (10)	0.5 (1)
M40	40	10	1 (10)	0.5 (1)
M60	60	20	4 (10)	0.5 (1)
M80	80	40	10	0.5
M100	100	40	10	0.8
HV40, HV60, HV80	40, 60, 80	N/A	10	0.5
MV4	4	0.05, $5 \times 10^{-4}$	10	0.5
MV60	60	0.05	10	0.5

**Table 1.** Overview of simulation parameters.

ping the simulation 100 Myr earlier or later. The drop at high gas surface densities in group H is due to the rapid collapse of our highly symmetric initial conditions and subsequent intense SN feedback in the absence of magnetic fields. This is visually demonstrated in Fig. 2, where the  $\Sigma_{\text{gas}} = 80 M_{\odot} \text{ pc}^{-2}$  M and H runs are shown side by side. We discuss this effect in detail in Sec. 3.3.1.

Comparing to results from other simulations, we find rough agreement with Rathjen et al. (2023) and Brucy et al. (2023a). While Kim et al. (2020a) show increased SFR at high values of  $\Sigma_{\text{gas}}$ , they vary the external gravitational potential represented by  $a_{\text{DM}}$  and  $a_{*}$  such that it increases as  $\Sigma_{\text{gas},0}$  increases, and therefore have an increased gas weight across their simulations. A fair comparison with Kim et al. (2020a) is made in terms of gas weight in Sec. 3.2, where we find good agreement with their results. Each of these works uses a different method when computing SFR. Kim et al. (2020a) average both SFR and  $\Sigma_{\text{gas}}$  over the period  $0.5 < t/t_{\text{orb}} < 1.5$ , where  $t_{\text{orb}}$  is the orbital time of the disk, which is equal to 220, 110, and 61 Myr, for a mean  $\Sigma_{\text{gas}}$  of 11, 30, and  $74 M_{\odot} \text{ pc}^{-2}$ . The shorter time used for the computation in the higher  $\Sigma_{\text{gas}}$  runs could lead to an artificial deviation from the observed KS relation, if, for example, a large burst of star formation happens to dominate the SFR in the sampled orbital time. Rathjen et al. (2023) average both gas surface density and SFR over the entire simulation run time, excluding the initial phase of turbulent driving, again giving times ranging from 250.5 Myr down to 114.6 Myr for the highest  $\Sigma_{\text{gas}}$

models, whose SFR is dominated by the initial burst of SFR. Brucy et al. (2023a) average the mass accreted onto sink particles over the period it takes their simulation to go from 97% to 60% of its initial gas mass, where gas is lost either via outflows or accretion onto sinks. This means that for the largest  $\Sigma_{\text{gas}}$  runs the period over which they calculate their SFR is  $\sim 100$  Myr for their TURB models. While these models differ from ours in several aspects, the agreement in the resulting KS relation is encouraging.

In Fig. 3, we bin individual simulation snapshots taken at 1 Myr intervals in  $\Sigma_{\text{gas}}-\Sigma_{\text{SFR}}$  space to create a 2D histogram version of the KS relation. For this analysis, we use results from groups M and H, substituting the runs with  $\Sigma_{\text{gas},0} \geq 40 M_{\odot} \text{ pc}^{-2}$  with runs from group HV. We also present a power law of the form  $\Sigma_{\text{gas}} \propto \Sigma_{\text{SFR}}^{1.7}$  normalized to the solar neighborhood value, for reference. Upon visual inspection, the three panels show a similar KS relation, with the H and HV runs presenting perhaps a larger scatter in  $\Sigma_{\text{SFR}}$ . The effect of magnetic fields on the scatter in the KS relation is further discussed in Sec. 3.3.

### 3.2. Vertical and Dynamical Equilibrium

In work by Ostriker et al. (2010) and Ostriker & Kim (2022, hereafter OK22), the formalism for pressure-regulated, feedback-modulated (PRFM) star-formation was established. In this picture, the mid-plane gas weight  $\mathcal{W}$  is balanced by the total mid-plane gas pressure  $P_{\text{tot}}$ , when averaged over time. In addition, the total pressure, and its magnetic, thermal, and turbulent

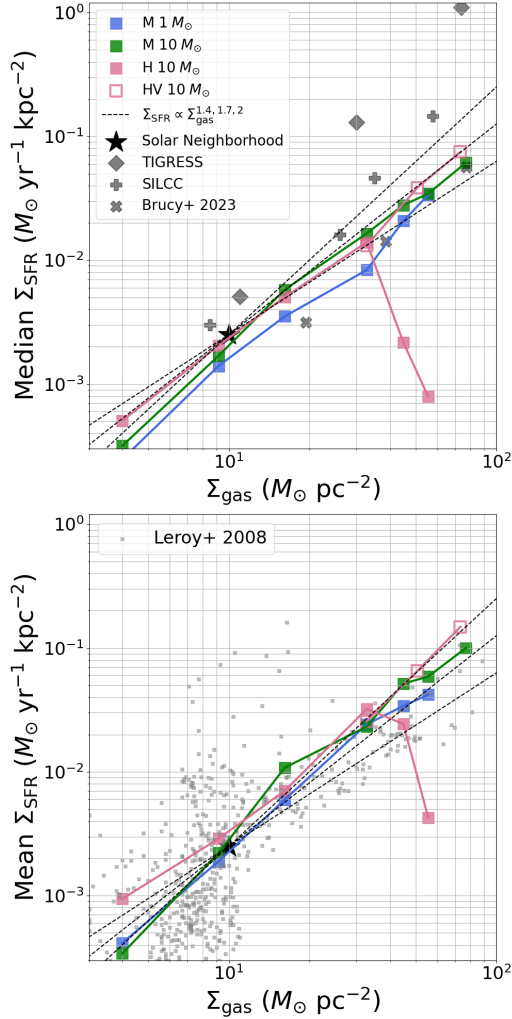


**Figure 1.** Median (top panel) and mean (bottom panel) binned values of  $\Sigma_{\text{SFR}}$  as a function of  $\Sigma_{\text{gas}}$  for groups H, M, and HV. Also plotted are observations from Leroy et al. (2008) and theoretical results from TIGRESS (Kim et al. 2020a), SILCC (Rathjen et al. 2023), and Brucy et al. (2023a).

components, can be related to the star formation rate surface density by the feedback yield  $\Upsilon$ , defined as

$$\Upsilon_i \equiv \frac{P_i}{\Sigma_{\text{SFR}}}, \quad (11)$$

where the index  $i$  represents the relevant pressure component (i.e., magnetic, thermal, turbulent, or the sum of all three). OK22 showed that  $\mathcal{W}$  and  $P_{\text{tot}}$  are well balanced in their high gas surface density MHD simulations. In addition, they show that the dynamical equilibrium pressure, defined as

$$P_{\text{DE}} \equiv \frac{\pi G \Sigma_{\text{gas}}}{2} + \Sigma_{\text{gas}} (2G\rho_{\text{sd}})^{1/2} \sigma_{\text{eff}}, \quad (12)$$

where  $\rho_{\text{sd}}$  is the mid-plane mass density of the stars and dark matter, and  $\sigma_{\text{eff}}$  is the effective velocity dispersion, is a good estimator for the total gas weight. The effective velocity dispersion is defined by

$$\sigma_{\text{eff}} \equiv \sqrt{c_s^2 + \sigma_B^2 + \sigma_z^2}, \quad (13)$$

where  $c_s$  is the sound speed,  $\sigma_B$  is given by  $\sqrt{(B^2 - B_z^2)/8\pi\rho}$  (i.e., the Alfvén velocity related to the  $x$ - and  $y$ - components of the magnetic field only), and  $\sigma_z$  is the standard deviation of the  $z$ -component of the gas velocity, all of which taken as the average across the entire box. In addition, the calculation of  $\sigma_{\text{eff}}$  is restricted to the warm and cold ISM, i.e., gas with  $T \leq 2 \times 10^4$  K. They compare the relation between  $\Sigma_{\text{SFR}}$  and  $P_{\text{DE}}$  in their simulations with observations, and compute the values of  $\Upsilon_i$  in their simulations as a function of  $P_{\text{DE}}$ . Kim et al. (2024) investigate the effect of metallicity and dust-to-gas ratio on feedback yields using their improved TIGRESS-NCR framework.

The top panel of Fig. 4 shows the relation between  $P_{\text{DE}}$  and the total mid-plane pressure, as measured by summing the mid-plane averages of  $P_{\text{th}}$ ,  $P_B$ , and  $P_{\text{turb}}$ . We perform volume-weighted averages, using the smoothing length  $\ell$  as an estimate of the particle size and  $\ell^3$  as weights. For the magnetic pressure, we consider only the component in the  $x$ - $y$  plane, while the turbulent pressure is taken to be  $\rho v_z^2$ , where  $v_z$  is the  $z$ -component of the particle velocity. Additionally, we average the resulting pressure over the period of 200-500 Myr. We find that our simulations fall within 30% of the one-to-one  $P_{\text{tot}}-P_{\text{DE}}$  relation. The exception is the HV80 run, with a surface density sufficiently high such that a pure hydrodynamical simulation does not exhibit vertical equilibrium. This is likely due to its gas spending most of the simulation time being driven out of- or falling back into the disk, with intermittent and very short star formation episodes. The bottom panel of Fig. 4 shows the relation between  $\Sigma_{\text{SFR}}$  and gas weight as represented by  $P_{\text{DE}}$ , as well as data from the PHANGS (Leroy et al. 2021; Sun et al. 2023) and EDGE-CALIFA (Barrera-Ballesteros et al. 2021; Wong et al. 2024) surveys. For comparison, we also plot the best fit based to simulations presented in Kim et al. (2024). Our results are in good agreement with observations, with the exception of higher  $\Sigma_{\text{SFR}}$  at low gas weights.

Our results show a similar  $\Sigma_{\text{SFR}}-P_{\text{DE}}$  slope to the Kim et al. (2024) fit, but an overall lower normalization. This difference is likely due to the resulting SN feedback, as it dominates the overall feedback yield. Several differences



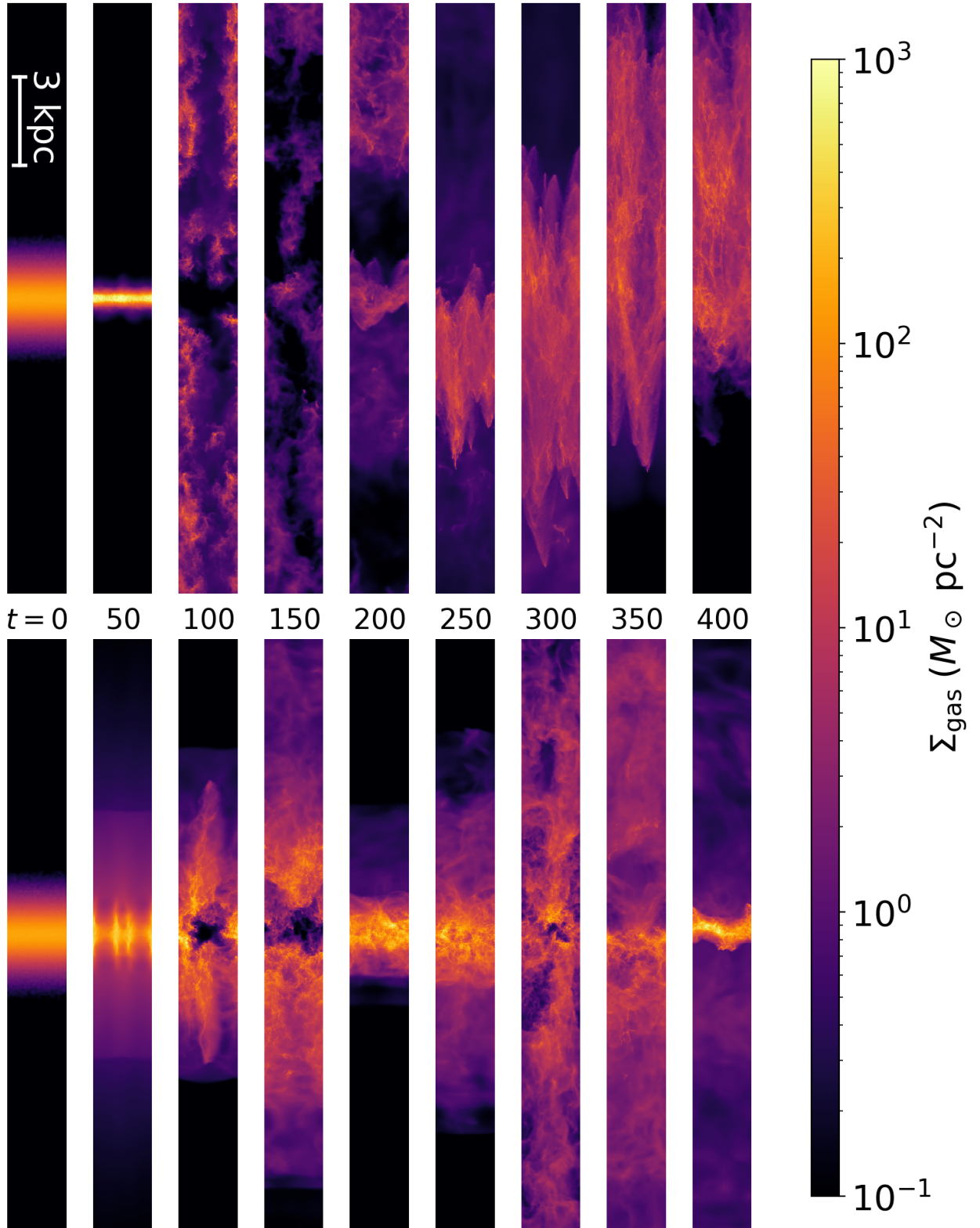


**Figure 2.** Edge-on gas surface density maps for snapshots at different times for simulations H80 (top row) and M80 (bottom row). Time is given in Myr.

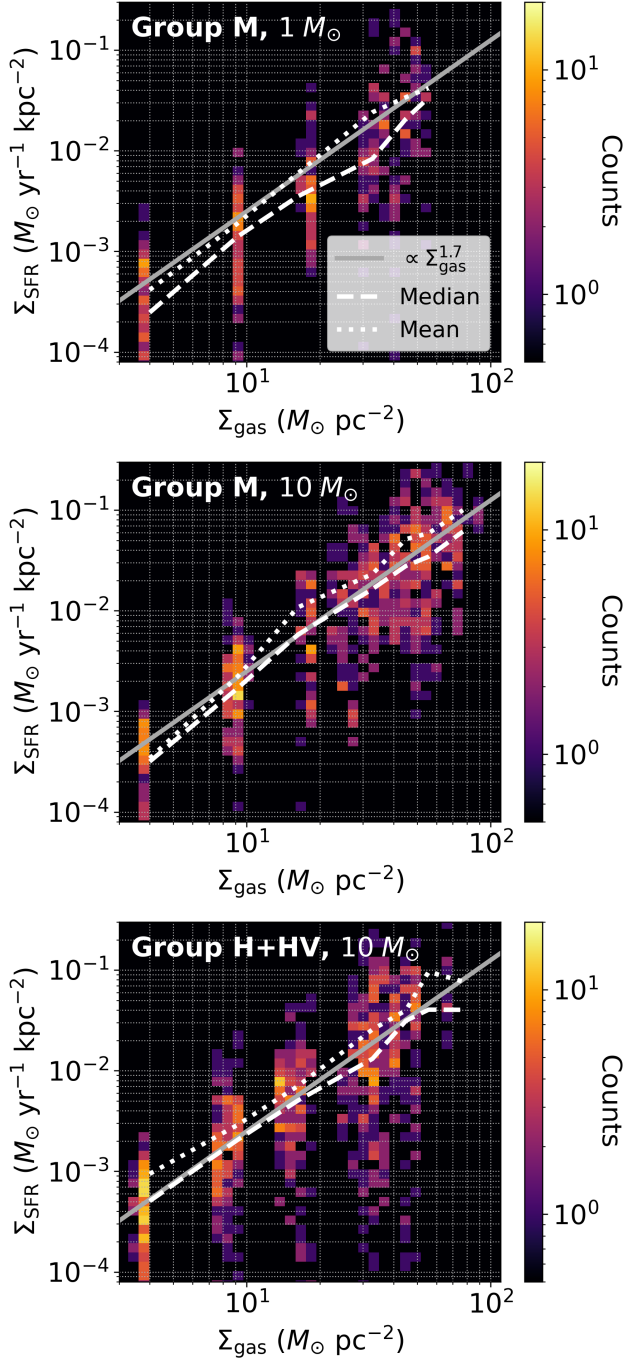


**Figure 3.** Time-resolved KS relation for our different simulation groups. We also plot the median and mean values of  $\Sigma_{\text{SFR}}$  binned along the  $\Sigma_{\text{gas}}$  axis, as well as a power law of the form  $\Sigma_{\text{gas}}^{1.7}$  for visual reference.

between our framework and the TIGRESS model could lead to this offset. The different choice of hydrodynamics code could change the efficiency of supernova bubble expansion. In addition, the different implementation of star particles and the inclusion of differential rotation

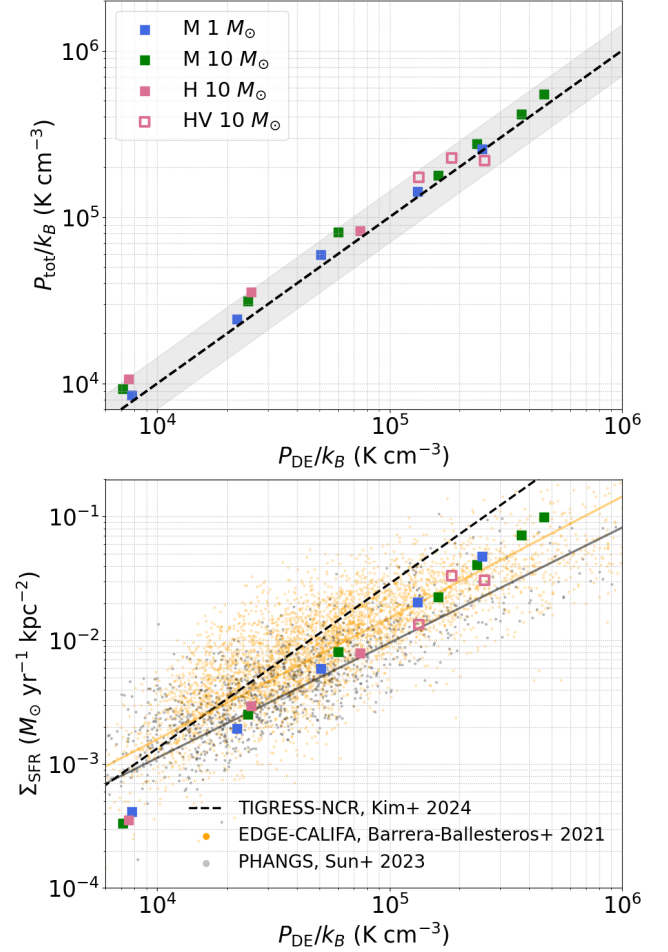


**Figure 4.** Top panel: mid-plane gas pressure as a function of the gas weight estimator  $P_{\text{DE}}$ , averaged over the period 200-500 Myr, for our different simulations. The dashed line shows the expected 1-to-1 relation, while the gray shaded region shows the  $\pm 30\%$  range. Bottom panel: star formation rate surface density as a function of  $P_{\text{DE}}$ , averaged over 200-500 Myr. The dashed line shows the fit to Kim et al. (2024). Points show observational data from the EDGE-CALIFA (Barrera-Ballesteros et al. 2021; Wong et al. 2024) and PHANGS surveys (Leroy et al. 2021; Sun et al. 2023), and the best fit to their data is shown in solid lines of the same color.

in TIGRESS could reduce the clustering of stars, leading to subsequently less clustered SNe and lowering the overall turbulent yield.

### 3.3. Effect of Magnetic Fields

#### 3.3.1. Disk Stabilization

Fig. 1 shows a drop in the KS relation for high gas surface densities in group H. The top row of Fig. 2 shows a sample of snapshots from the H80 run. For almost 500 Myr, the gas never forms a quasi-steady disk structure,

and is therefore prevented from forming stars. This is a result of our initial conditions, which are symmetrical in the  $x$ - and  $y$ - directions. Following the initial collapse of the disk, star formation peaks simultaneously across the box mid-plane, and the subsequent SN feedback is so intense that almost half of the gas is driven out of the box. The remaining gas acquires such a high velocity that it oscillates about the box mid-plane until it begins to settle into a disk at  $t = 500$  Myr.

It has been demonstrated that this initial burst of star formation and subsequent feedback can be moderated by a combination of magnetic pressure and artificially driving turbulence for an initial time period until stars begin to form (see, e.g., Kim & Ostriker 2017; Rathjen et al. 2023; Brucy et al. 2023a). We do not externally drive turbulence in any of our simulations. In contrast to the H80 run, in the M80 run, shown in the bottom row of Fig. 2, magnetic fields slow down the initial collapse of the disk, and effectively create inhomogeneities in the mid-plane. This inhibits the initial extreme burst of star formation, allowing a quasi-steady disk to form. Thus, simulating a kpc-scale ISM without magnetic fields requires mitigation of this initial burst. We find that setting the initial gas distribution as we do for group HV is sufficient to achieve a successful pure hydrodynamical simulation up to  $\Sigma_{\text{gas},0} = 80 M_{\odot} \text{ pc}^{-2}$ . This allows us to directly compare between hydrodynamical and MHD simulations in the high column density regime.

### 3.3.2. Magnetic Support

In addition to reducing the strength of SN feedback that dominates in the first  $\sim 200$  Myr of our simulations, magnetic fields also affect the evolution and structure of the ISM. To compare the importance of the magnetic and thermal pressure in star-forming gas, we define  $\beta_{\text{th},100}$  to be the mass-weighted plasma  $\beta$  parameter, averaged over gas particles with volume density  $n > 100 \text{ cm}^{-3}$ . The top panel of Fig. 5 shows the relationship between  $\beta_{\text{th},100}$  and the time-averaged  $\Sigma_{\text{gas}}$  taken over a simulation time of 200–500 Myr, demonstrating a clear decreasing trend. In the dense gas, which tends to be cold, magnetic pressure is non-negligible already at low  $\langle \Sigma_{\text{gas}} \rangle$  and becomes increasingly dominant as  $\langle \Sigma_{\text{gas}} \rangle$  increases. In addition, there is a systematic trend with resolution, where  $\beta_{\text{th},100}$  is lower for higher resolution.

Repeating this analysis for the turbulent pressure component, we define  $\beta_{\text{turb}}$  as the ratio between the turbulent and magnetic pressure in the box mid-plane. To calculate  $\beta_{\text{turb}}$ , we first partition the box mid-plane, de-

fining by  $|z| < 10 \text{ pc}$ , into cubes with a side length of 10 pc. For each cube, we calculate the mass-weighted Alfvén velocity  $\sigma_B$ , and the standard deviation of the  $z$ -component of the gas velocity  $\sigma_z$ . We then calculate  $\beta_{\text{turb}}$  by taking the mass-weighted average of the ratio  $(\sigma_z/\sigma_B)^2$  across all of these sub-volumes over a simulation time of 200–500 Myr. We do not restrict  $\beta_{\text{turb}}$  to dense cubes, as very few regions would fulfill the  $n > 100$  criterion and the results would become quite noisy due to averaging over a small number of regions. Similar to  $\beta_{\text{th},100}$ , the bottom panel of Fig. 5 shows that  $\beta_{\text{turb}}$  decreases with increasing  $\langle \Sigma_{\text{gas}} \rangle$  and with improved resolution. This method of comparing turbulent and magnetic support is more precise when discussing turbulent pressure support on the scale of individual clouds. The (volume-weighted) average of  $\sigma_{\text{turb}}$  over the entire simulation volume is still the appropriate quantity when discussing vertical pressure support and dynamical equilibrium on the scale of the entire disk (see Appendix A). Both of these results are consistent with magnetic pressure playing an important role in supporting the cold ISM on cloud scales against gravitational collapse, with growing importance as the gas surface density increases.

Since magnetic pressure in star-forming gas in our simulations becomes increasingly important as the gas surface density increases, we can expect star-forming clouds to collapse faster in high  $\Sigma_{\text{gas},0}$  runs when magnetic fields are turned off. However, when averaged over large timescales, the SFR is not affected. This is demonstrated in Sec. 3.1 for simulations that successfully form quasi-steady disks, which indeed occurs in all of our models excluding H80. In these cases, feedback-induced self-regulation always drives our simulations towards the observed KS relation.

Fig. 6 shows the burstiness parameter for our low-resolution models, defined following Zhang et al. (2024) as

$$\text{Burstiness} = \frac{\sigma(\text{SFR})}{\langle \text{SFR} \rangle} \quad (14)$$

where SFR is computed as is described in Sec. 3.1, and  $\langle \text{SFR} \rangle$  is averaged over the simulation time between 200–500 Myr, and  $\sigma(\text{SFR})$  is the standard deviation of the SFR in that period. We compare groups M, H, and HV, and find that simulations from groups H and V are burstier than group M, and that, except for  $\Sigma_{\text{gas},0} = 60 M_{\odot} \text{ pc}^{-2}$ , generally follow a trend where higher surface density leads to burstier star formation. Additionally, the difference in burstiness between groups H/HV and group M increases with gas surface density. Fig. 7 shows the time-averaged effective disk height,  $H_d$ ,

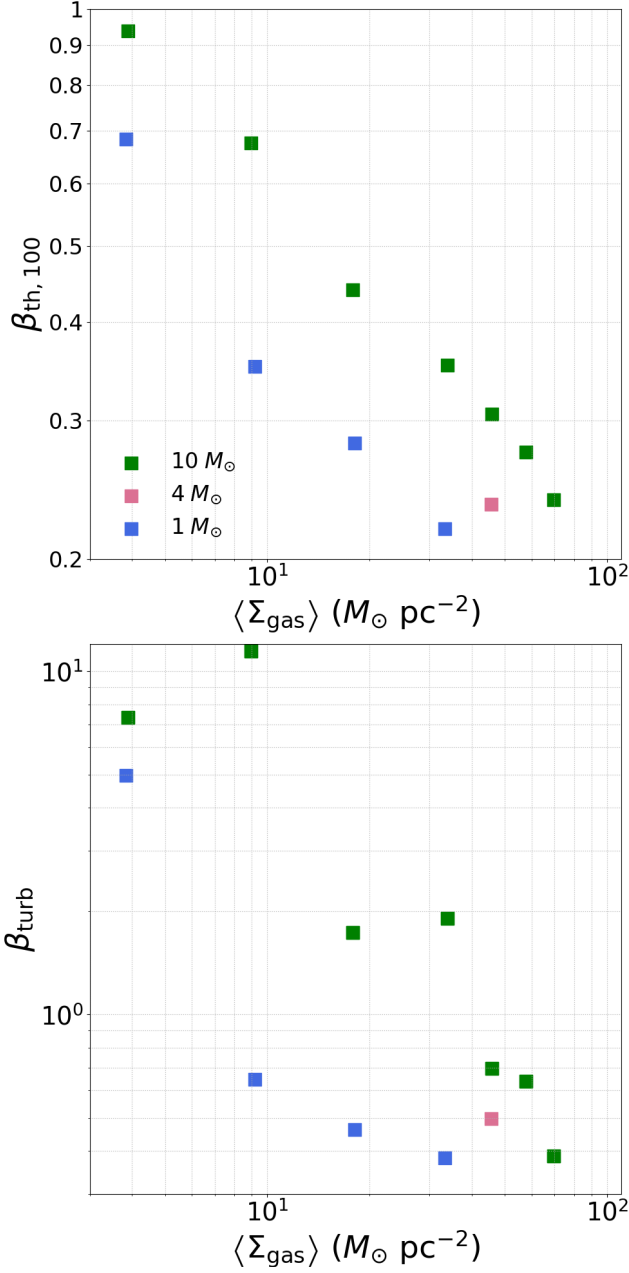


**Figure 5.** Top panel:  $\beta_{\text{th},100}$  in our M models, defined as the mass-weighted plasma  $\beta$  parameter averaged over gas particles with volume density  $n > 100 \text{ cm}^{-3}$ , as a function of the time averaged gas surface density  $\langle \Sigma_{\text{gas}} \rangle$ . Bottom panel: same as top panel, but for  $\beta_{\text{turb}}$ , the ratio between turbulent and magnetic pressure measured on 10 pc scales.

defined as the distance from the mid-plane in which 50% of the gas mass is contained. We can see that there is a general increasing trend in disk height with gas surface density, and that the disk height is larger at a given gas surface density in group H and HV, compared to group M. Moreover, the difference is larger for higher

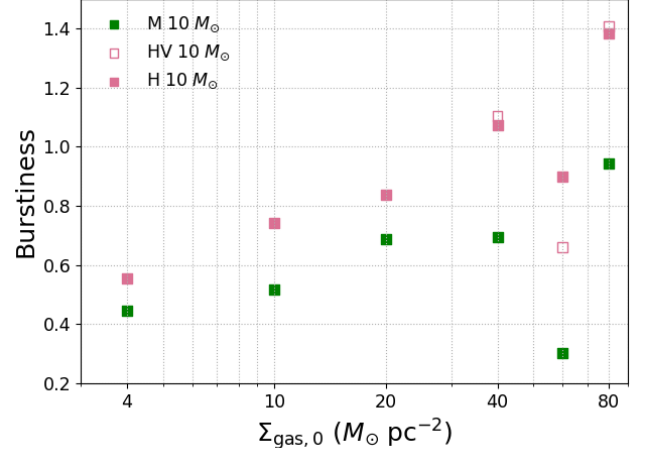


**Figure 6.** Burstiness parameter, defined as  $\frac{\sigma(\text{SFR})}{\langle \text{SFR} \rangle}$ , as a function of  $\Sigma_{\text{gas},0}$ , for our low-resolution models.

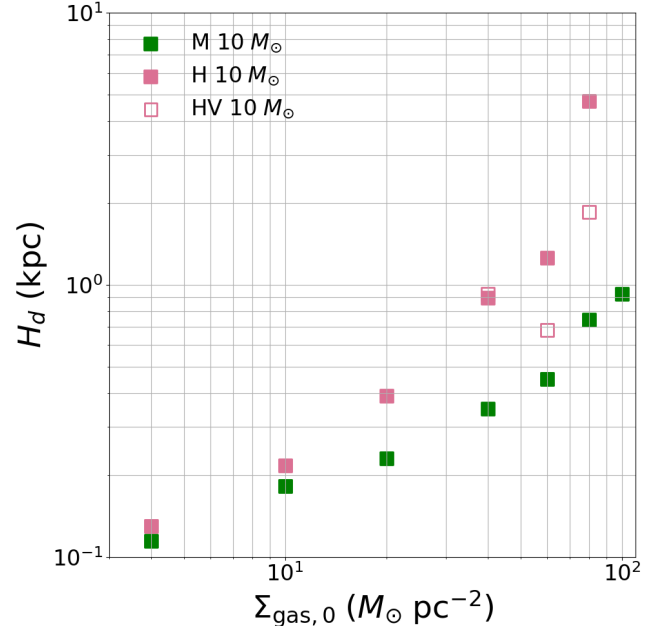


**Figure 7.** Effective disk-height as a function of  $\Sigma_{\text{gas},0}$  for our  $10 M_{\odot}$  models in Groups M, H, and HV.

$\Sigma_{\text{gas},0}$ . The increase in burstiness and disk height can be explained by the fact that in the absence of magnetic fields, the faster collapse can lead to more stars forming from a single gas cloud before being dispersed by eventual SN feedback. The resulting SN feedback from a larger cluster of stars will then be stronger and more effective, and will drive more gas further out of the disk mid-plane. This, in turn, increases the effective disk height, as well as the gas outflow rate. We defer a full investigation of the effect of gas surface density and

magnetic fields on the energy- and mass-loading factors to a future study.

### 3.3.3. ISM Phase Distribution

Fig. 8 shows the ISM phase distribution in our models as a function of  $\Sigma_{\text{gas},0}$ . We plot the mass fractions of the cold gas, warm neutral medium (WNM), and hot ionized medium (HIM) within 300 pc of the box mid-plane. We choose this region by calculating the star formation height  $H_{\text{SF}}$ , which is defined as the mid-plane distance within which half of the mass in stars with an age less than  $t_{\text{SF}}$  is contained. We inspect the temporal variation of  $H_{\text{SF}}$  across all of our models and find that it does not exceed 300 pc, making it a good definition for the region in the box where star-forming gas resides. We assign gas particles to each phase according to temperature and ionization fraction:  $T < 300$  K for cold gas,  $300 < T < 15,000$  K and  $x_e < 0.9$  for WNM, and  $T > 15,000$  K for HIM. Our results are insensitive to the small changes in the temperature boundary between our WNM and HIM definitions, as the WNM mostly occupies a very narrow temperature range at  $\sim 10,000$  K, and the HIM is mostly at temperatures  $\gtrsim 10^6$  K. In addition, our definition of WNM includes thermally unstable neutral gas. We require that the WNM has an ionization fraction  $< 0.9$  in order to remove gas associated with HII regions, although these do not constitute more than 1% of the mass in any of our models.

For models in group M, we find an increase in the cold gas fraction,  $f_{\text{cold}}$ , as we increase the  $\Sigma_{\text{gas},0}$ . Additionally, we find that  $f_{\text{cold}}$  increases at higher resolution by almost 10% where the resolution is increased by a factor of 10. For  $\Sigma_{\text{gas},0} = 60 M_{\odot} \text{ pc}^{-2}$ , our high-resolution gas particle mass is  $4 M_{\odot}$ , hence the smaller difference between the high- and low-resolution models.

A similar trend with  $\Sigma_{\text{gas},0}$  exists for groups H and HV for  $\Sigma_{\text{gas},0} \leq 60 M_{\odot} \text{ pc}^{-2}$ . However, we find a drop in  $f_{\text{cold}}$  in both the H80 and HV80 models. In the H80 model, the decrease in  $f_{\text{cold}}$  is compensated for by an increase in  $f_{\text{WNM}}$ . This can be understood as part of the effect of our initial conditions, and the absence of a quasi-steady disk forming (see Sec. 3.3.1). The gas simply never settles into a disk, and therefore does not compress, cool, or form stars efficiently, but rather remains in a WNM-dominated state while oscillating about the box mid-place. As we show in Fig. 1, the HV80 model does form stars as expected from its gas surface density. Even so, we find that it has lower  $f_{\text{cold}}$  than its M80 counterpart, and even lower than H60. The decrease in  $f_{\text{cold}}$  is compensated for by an increase in  $f_{\text{HIM}}$ . As the

HIM is formed by SN shock heating, this demonstrates that while magnetic fields may not affect the SFR when averaged over long times, they do play an important role in how SN feedback shapes the ISM phase structure.

The reason for the increase in the cold gas fraction when  $\Sigma_{\text{gas},0}$  is increased is once again the magnetic pressure, which becomes increasingly important as the gas surface density increases. As it slows down the collapse of cold, star-forming, gas clouds, it allows cold gas to survive for a longer period before the onset of feedback which consequently destroys the cloud. This means that correctly modeling magnetic fields in the ISM is crucial for the study of the cold ISM, and particularly the study of emission lines that trace cold gas, such as CO rotational lines, [C I] 640 and 390  $\mu\text{m}$ , and [C II] 158  $\mu\text{m}$ , although the origin of the latter could be in other phases of the ISM (see, e.g. Gurman et al. 2024). The strength of these lines, which dominate cooling in the cold ISM, directly depends on how much of the ISM mass is in the cold and dense phase at a fixed SFR. Thus, modeling these lines to study the relationship between emission, cold or molecular gas mass, and star formation, is likely strongly affected if magnetic fields are ignored.

## 4. STEADY STATE MAGNETIC FIELD

In this section, we demonstrate that a steady-state magnetic field emerges in our simulation, whose value is determined by the gas surface density.

### 4.1. B-field Independence of Initial Conditions

Fig. 9 shows the mass-weighted magnetic field in the dense gas ( $n > 100 \text{ cm}^{-3}$ ) gas, denoted as  $B_{100}$ , as a function of time for an additional set of simulations listed in Tab. 2. These simulations were run with magnetic fields turned on and with an identical setup to Group M (black and red curves) or MV (blue curves), the only difference being the value of  $B_0$ . We also apply a moving average with a window of 200 Myr to  $B_{100}$  as its fluctuations in time (of order 1 dex) qualitatively follow the fluctuations in SFR, and obscure its convergence. The red lines mark our fiducial models which we use for the analysis in the rest of the paper (group M). In all cases, we find that variations in the initial magnetic field by up to 4 orders of magnitude, and the initial orientation of the magnetic field, all result in variations in the steady-state value of  $B_{100}$  by less than a factor of  $\sim 2$ . In the  $\Sigma_{\text{gas},0} = 4 M_{\odot} \text{ pc}^{-2}$  case, we find that this convergence takes a longer time, of the order of a few 100 Myr. If the setting of  $B_{100}$  is related to SN driven turbulence, then we can associate this slower convergence

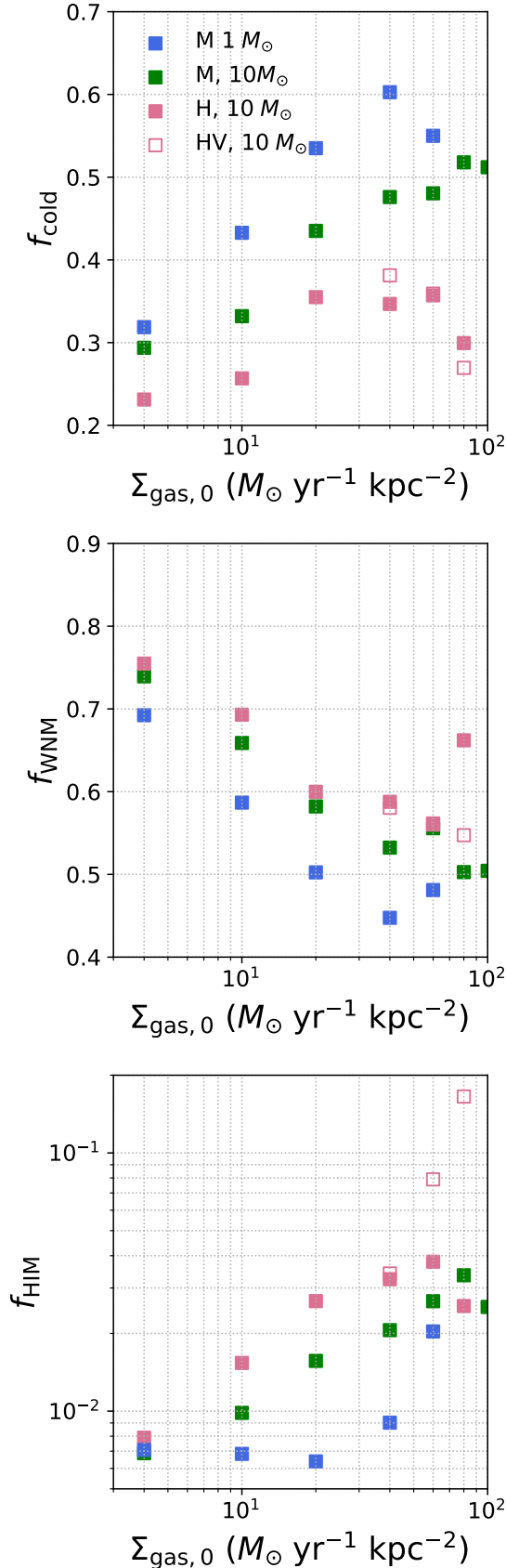


**Figure 8.** Time averaged mass fraction of cold gas, WNM, and HIM, within 300 pc of the box mid-plane.

$\Sigma_{\text{gas}}$ (a)	$B_0$ (b)	$B_{100,\text{final}}$ (c)	$\Sigma_{\text{SFR}}$ (d)
4	5	7.62	2.53
	0.5	9.88	2.58
	0.05	6.73	3.70
*	0.05	6.48	5.04
*	$5 \times 10^{-4}$	4.80	5.85
10	5	15.3	18.9
	0.5	13.6	23.1
	0.05	11.2	29.1
40	50	22.3	178
	10	21.8	238
	5	14.9	168
60	20	32.6	334
	5	25.8	176
*	0.05	19.9	194

**Table 2.** List of our simulation runs with different values of  $B_0$ . Simulations use our group M setup, except for rows marked by an asterisk which use our group MV setup. Values are given in units of (a)  $M_{\odot} \text{ pc}^{-2}$ , (b)  $\mu\text{G}$ , (c)  $\mu\text{G}$ , (d)  $10^{-4} M_{\odot} \text{ kpc}^{-2} \text{ yr}^{-1}$ .

of  $B_{100}$  to the lower SFR in  $\Sigma_{\text{gas},0} = 4 M_{\odot} \text{ pc}^{-2}$  models. Our  $\Sigma_{\text{gas},0} = 10 M_{\odot} \text{ pc}^{-2}$  models take  $\sim 100$  Myr to stabilize, while  $\Sigma_{\text{gas},0} = 40$  and  $60 M_{\odot} \text{ pc}^{-2}$  achieve convergence almost instantly, all in line with the convergence time being related to SFR. In Tab. 2 we show  $B_0$ , as well as the values of  $B_{100}$  and  $\Sigma_{\text{SFR}}$ , both averaged over the last 200 Myr of the simulation, for the different tests shown in Fig. 9. We see that even when  $B_0$  is varied by orders of magnitude,  $B_{100}$  reaches the same steady state value of order  $\sim 10 \mu\text{G}$ , to within a factor of  $\sim 2$ , and the SFR is also weakly affected.

#### 4.2. $B - \Sigma_{\text{gas}}$ Relation

Given that our tests show that our  $B_{100}$  emerges from our simulations independently of our initial conditions, we can investigate the relationship between the  $B_{100}$  and  $\Sigma_{\text{gas}}$ . Fig. 10 shows our time-resolved  $B_{100} - \Sigma_{\text{gas}}$  relation. We plot the 2-dimensional histogram as well as the binned mean and median values of  $B_{100}$ , and a power law of the form  $B \propto \Sigma^{0.5}$ .

Fig. 11 shows the average relation between the magnetic field strength and gas density for group M. We calculate the relation by taking simulation data between times 200 and 500 Myr, binning particles according to

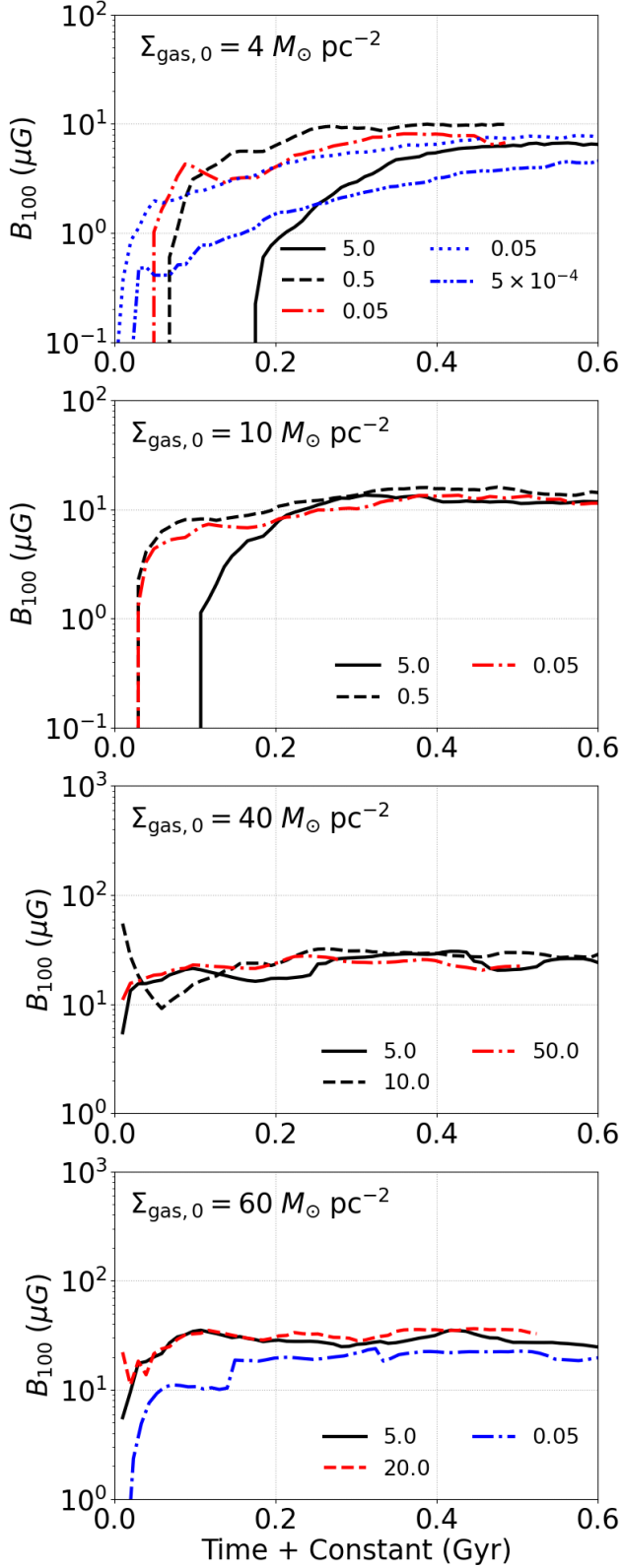


**Figure 9.** Mass-weighted mean  $B_{100}$  as a function of time. Each panel shows simulations with a single value of  $\Sigma_{\text{gas},0}$  indicated in the upper left corner of each panel. The value of  $B_0$  is given in the legend in  $\mu\text{G}$ .  $B_{100}$  is smoothed using a 200 Myr window in order to visually demonstrate its convergence. Red lines denote our group M runs, blue lines denote our group MV runs.

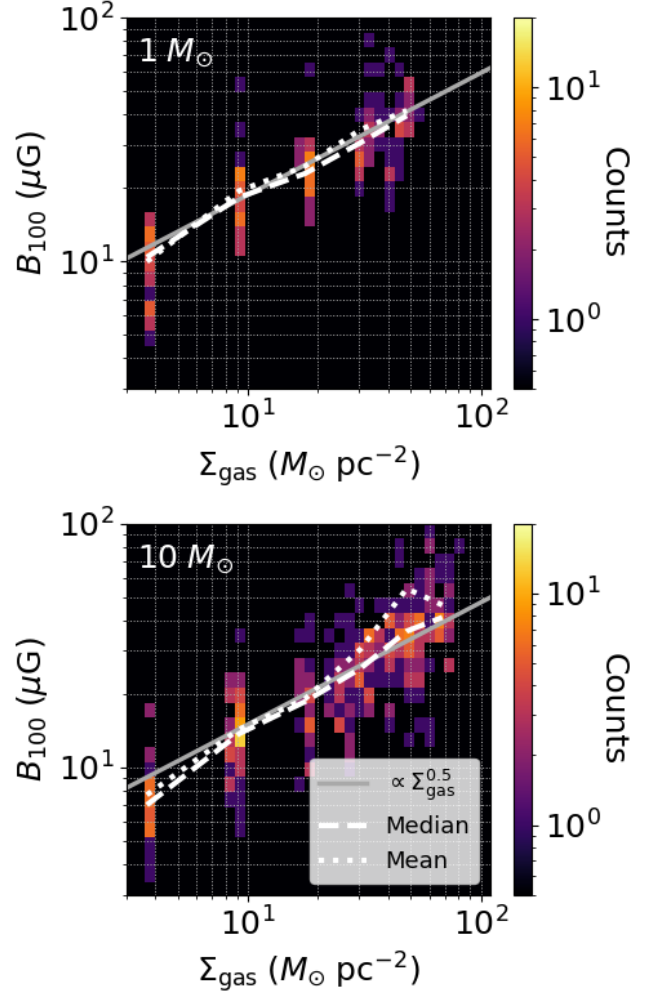


**Figure 10.** Time-resolved  $B_{100}$ - $\Sigma_{\text{gas},0}$  relation for simulations in group M at a resolution of  $1 M_{\odot}$  (top panel) and  $10 M_{\odot}$  (bottom panel).

density, and taking the mass-weighted magnetic field strength in each bin. We find that at high densities, the average magnetic field is higher at a given density for higher values of  $\Sigma_{\text{gas},0}$ . The  $B$ - $n$  relation also follows a power law with a slope of  $\sim 0.4$ , close to the slope predicted from theory and simulations of the collapse of strongly magnetized dense clouds (Padoan & Nordlund 1999). In the low-density gas, we find that the  $B$ - $n$  relation roughly follows a power law dependence with a slope of  $2/3$ , as is expected in the flux-freezing limit. We do see some of the curves intersecting at low densities, perhaps due to a dependence of the magnetic field in the diffuse phase on our initial conditions. This should not affect the dynamics of the simulation, as magnetic pressure is negligible compared to the thermal pressure at these low densities.

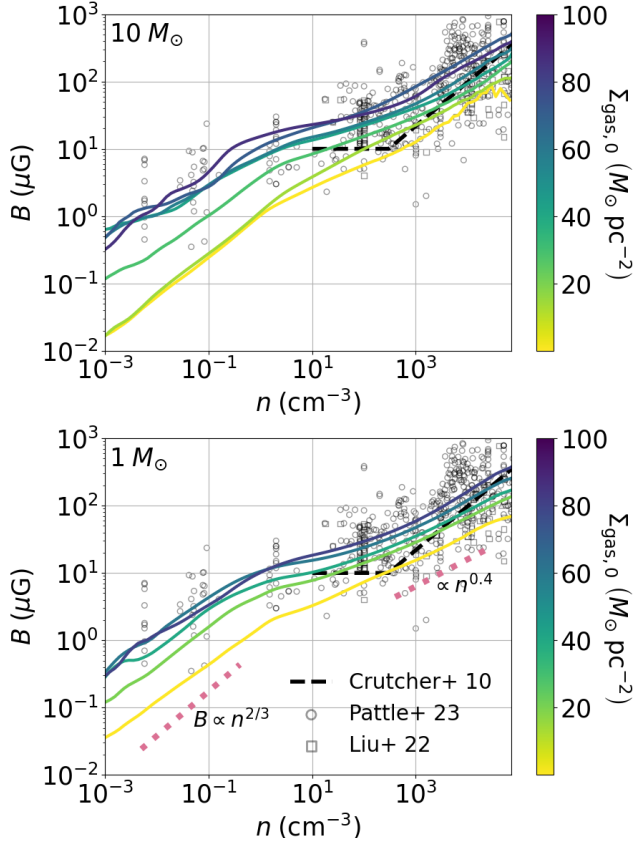


**Figure 11.** Mean magnetic field as a function of gas density for simulations in group M. Mass resolution is specified in the upper left of each panel, and  $\Sigma_{\text{gas},0}$  is specified by the color of the curve. In addition, we plot the broken power law fit to observations of Crutcher et al. (2010), and the data points from Liu et al. (2022) and Pattle et al. (2023). We also plot power laws with a slope of 0.6 and 0.4 for reference.

The fact that the normalization of the  $B$ - $n$  relation in the dense gas is higher at higher  $\Sigma_{\text{gas},0}$  demonstrates that the driver of our  $B_{100-\Sigma_{\text{gas}}}$  relation is not an increase in the amount of dense gas, but rather that the physical mechanism that sets the magnetic field (in the dense gas) is connected to the gas surface density. A natural explanation is that as the gas surface density increases, so does the star-formation rate surface density and, in turn, the SN rate surface density. This leads to increased turbulence, which then amplifies the magnetic field to higher values through the small-scale dynamo effect. We note that while a discussion of the amplification mechanism of the magnetic field is beyond the scope of this work, our results are roughly consistent with SN-driven turbulent dynamo where the growth rate of magnetic fields is captured by the  $\mathbf{v} \times \mathbf{B}$  term in the induction equation, while the saturation is driven by the numerical dissipation of our code.

## 5. SUMMARY

We have presented a new suite of high-resolution (1-10  $M_{\odot}$ ,  $\sim 0.2$ - $0.4$  pc) 3D simulations of a galactic patch, with a resolved cold ISM, star-by-star treatment of star formation, SN and photoionization feedback. Our models span a wide range in gas surface density, and, for the first time, include successful pure hydrodynamical simulations at high gas surface densities, running for 500 Myr or more. This has allowed us to capture the evolution and importance of magnetic fields in this column density regime.

1. Our KS relation agrees with observations and other theoretical work, with a power law index in the 1.4-1.7 range.
2. Our simulations are in vertical dynamical equilibrium. The relation between  $\Sigma_{\text{SFR}}$  and total gas weight in our simulations is in good agreement with observations, and agrees with the TIGRESS-NCR simulations (Kim et al. 2024) to within a factor  $\sim 2$ .
3. We find that magnetic fields play an important role at the high gas surface density regime ( $\Sigma_{\text{gas}} \gtrsim 40 M_{\odot} \text{ pc}^{-2}$ ), by reducing the strong fluctuations in SFR which are prevalent in the pure-hydrodynamical models, but without changing the SFR when averaged over long times.
4. As a result, simulations with magnetic fields show a 10%–25% increase in cold gas fraction and a reduction in disk scale height by up to a factor of 3.
5. Magnetic fields help mitigate the initial strong burst of star formation known to occur in galactic patch simulations. We demonstrate that this mitigation can also be achieved by using more mixed initial conditions, as we do in group HV.
6. We find that the magnetic field strength in the dense gas is insensitive to the initial magnetic field strength and configuration, and that a  $\Sigma_{\text{gas}}$ -dependent, quasi-steady state magnetic field strength emerges from our simulations, approximately following a power law of the form  $B \propto \Sigma_{\text{gas}}^{0.5}$ .
7. The  $B$ - $n$  relation in our models shows a power law slope of 2/3 and 0.4 in the diffuse and dense regimes, respectively. The normalization of the relation changes with the gas surface density, in agreement with observations despite the large scatter. This points to the magnetic field strength being set by SN-driven small-scale dynamo.
8. Future prospects for analysis based on the GHOSDT simulations are abundant. These include the effect of  $\Sigma_{\text{gas}}$  on chemical abundances, ISM phase structure,



outflow statistics, and line emission from atomic and molecular gas. In addition, we now have the capability to compare pure hydrodynamical simulations with their MHD counterparts. Finally, the extension into even higher values of  $\Sigma_{\text{gas}}$  could help shed light on the gas properties of gas-rich starburst galaxies and the high star formation efficiencies observed in the brightest galaxies in the early universe.

We thank Chang-Goo Kim and Eve C. Ostriker for fruitful discussions. We thank Kate Pattle and Jorge K. Barrera-Ballesteros for sharing observational data sets. This work was supported by the German Science Foundation via DFG/DIP grant STE/1869-2 GE 625/17-1, by the Center for Computational Astrophysics (CCA) of the Flatiron Institute, and the Mathematics and Physical Sciences (MPS) division of the Simons Foundation, USA.

## REFERENCES

- Andersson, E. P., Agertz, O., & Renaud, F. 2020, *Monthly Notices of the Royal Astronomical Society*, 494, 3328, doi: [10.1093/mnras/staa889](https://doi.org/10.1093/mnras/staa889)
- Andersson, E. P., Agertz, O., Renaud, F., & Teyssier, R. 2023, *Monthly Notices of the Royal Astronomical Society*, 521, 2196, doi: [10.1093/mnras/stad692](https://doi.org/10.1093/mnras/stad692)
- Andersson, E. P., Rey, M. P., Pontzen, A., et al. 2024. <https://arxiv.org/abs/2409.08073>
- Barnes, J., & Hut, P. 1986, *Nature*, 324, 446, doi: [10.1038/324446a0](https://doi.org/10.1038/324446a0)
- Barrera-Ballesteros, J. K., Sánchez, S. F., Heckman, T., et al. 2021, *MNRAS*, 503, 3643, doi: [10.1093/mnras/stab755](https://doi.org/10.1093/mnras/stab755)
- Bigieli, F., Leroy, A., Walter, F., et al. 2008, *AJ*, 136, 2846, doi: [10.1088/0004-6256/136/6/2846](https://doi.org/10.1088/0004-6256/136/6/2846)
- Brucy, N., Hennebelle, P., Colman, T., & Iteanu, S. 2023a, *A&A*, 675, A144, doi: [10.1051/0004-6361/202244915](https://doi.org/10.1051/0004-6361/202244915)
- . 2023b, *A&A*, 675, A144, doi: [10.1051/0004-6361/202244915](https://doi.org/10.1051/0004-6361/202244915)
- Calura, F., Lupi, A., Rosdahl, J., et al. 2022, *MNRAS*, 516, 5914, doi: [10.1093/mnras/stac2387](https://doi.org/10.1093/mnras/stac2387)
- Cardelli, J. A., Meyer, D. M., Jura, M., & Savage, B. D. 1996, *ApJ*, 467, 334, doi: [10.1086/177608](https://doi.org/10.1086/177608)
- Crutcher, R. M., Wandelt, B., Heiles, C., Falgarone, E., & Troland, T. H. 2010, *ApJ*, 725, 466, doi: [10.1088/0004-637X/725/1/466](https://doi.org/10.1088/0004-637X/725/1/466)
- de Avillez, M., & Breitschwerdt, D. 2004, *Ap&SS*, 289, 479, doi: [10.1023/B:ASTR.0000014981.50094.8f](https://doi.org/10.1023/B:ASTR.0000014981.50094.8f)
- Dedner, A., Kemm, F., Kröner, D., et al. 2002, *Journal of Computational Physics*, 175, 645, doi: [10.1006/jcph.2001.6961](https://doi.org/10.1006/jcph.2001.6961)
- Deng, Y., Li, H., Liu, B., et al. 2024, arXiv e-prints, arXiv:2405.08869, doi: [10.48550/arXiv.2405.08869](https://doi.org/10.48550/arXiv.2405.08869)
- Emerick, A., Bryan, G. L., & Mac Low, M.-M. 2019, *MNRAS*, 482, 1304, doi: [10.1093/mnras/sty2689](https://doi.org/10.1093/mnras/sty2689)
- . 2020a, arXiv e-prints, arXiv:2007.03702, doi: [10.48550/arXiv.2007.03702](https://doi.org/10.48550/arXiv.2007.03702)
- . 2020b, *ApJ*, 890, 155, doi: [10.3847/1538-4357/ab6efc](https://doi.org/10.3847/1538-4357/ab6efc)
- Fotopoulou, C. M., Naab, T., Lahén, N., et al. 2024, *MNRAS*, 534, 215, doi: [10.1093/mnras/stae2072](https://doi.org/10.1093/mnras/stae2072)
- Fuchs, B., Jahreiß, H., & Flynn, C. 2009, *AJ*, 137, 266, doi: [10.1088/0004-6256/137/1/266](https://doi.org/10.1088/0004-6256/137/1/266)
- Fujii, M. S., Hattori, K., Wang, L., et al. 2022a, *MNRAS*, 514, 43, doi: [10.1093/mnras/stac808](https://doi.org/10.1093/mnras/stac808)
- Fujii, M. S., Saitoh, T. R., Hirai, Y., & Wang, L. 2021a, *PASJ*, 73, 1074, doi: [10.1093/pasj/psab061](https://doi.org/10.1093/pasj/psab061)
- Fujii, M. S., Saitoh, T. R., Wang, L., & Hirai, Y. 2021b, *PASJ*, 73, 1057, doi: [10.1093/pasj/psab037](https://doi.org/10.1093/pasj/psab037)
- Fujii, M. S., Wang, L., Hirai, Y., et al. 2022b, *MNRAS*, 514, 2513, doi: [10.1093/mnras/stac1496](https://doi.org/10.1093/mnras/stac1496)
- Fujii, M. S., Wang, L., Tanikawa, A., Hirai, Y., & Saitoh, T. R. 2024, *Science*, 384, 1488, doi: [10.1126/science.adi4211](https://doi.org/10.1126/science.adi4211)
- Gaburov, E., & Nitadori, K. 2011, *MNRAS*, 414, 129, doi: [10.1111/j.1365-2966.2011.18313.x](https://doi.org/10.1111/j.1365-2966.2011.18313.x)
- Girichidis, P., Seifried, D., Naab, T., et al. 2018, *MNRAS*, 480, 3511, doi: [10.1093/mnras/sty2016](https://doi.org/10.1093/mnras/sty2016)
- Girichidis, P., Walch, S., Naab, T., et al. 2015, eprint arXiv:1508.06646. <http://adsabs.harvard.edu/abs/2015arXiv150806646G>
- Glover, S. C. O., & Clark, P. C. 2012, *MNRAS*, 421, 116, doi: [10.1111/j.1365-2966.2011.20260.x](https://doi.org/10.1111/j.1365-2966.2011.20260.x)
- Glover, S. C. O., & Mac Low, M. 2007, *ApJS*, 169, 239, doi: [10.1086/512238](https://doi.org/10.1086/512238)
- Górski, K. M., & Hivon, E. 2011, HEALPix: Hierarchical Equal Area isoLatitude Pixelization of a sphere, *Astrophysics Source Code Library*. <http://ascl.net/1107.018>
- Gressel, O., Elstner, D., Ziegler, U., & Rüdiger, G. 2008, *A&A*, 486, L35, doi: [10.1051/0004-6361/200810195](https://doi.org/10.1051/0004-6361/200810195)
- Grudić, M. Y., Guszejnov, D., Hopkins, P. F., Offner, S. S. R., & Faucher-Giguère, C.-A. 2021, *MNRAS*, 506, 2199, doi: [10.1093/mnras/stab1347](https://doi.org/10.1093/mnras/stab1347)
- Grudić, M. Y., Guszejnov, D., Offner, S. S. R., et al. 2022, *MNRAS*, 512, 216, doi: [10.1093/mnras/stac526](https://doi.org/10.1093/mnras/stac526)

- Gurman, A., Hu, C.-Y., Sternberg, A., & van Dishoeck, E. F. 2024, *ApJ*, 965, 179, doi: [10.3847/1538-4357/ad2eac](https://doi.org/10.3847/1538-4357/ad2eac)
- Gutcke, T. A., Pakmor, R., Naab, T., & Springel, V. 2021, *MNRAS*, 501, 5597, doi: [10.1093/mnras/staa3875](https://doi.org/10.1093/mnras/staa3875)
- . 2022a, *MNRAS*, 513, 1372, doi: [10.1093/mnras/stac867](https://doi.org/10.1093/mnras/stac867)
- Gutcke, T. A., Pfrommer, C., Bryan, G. L., et al. 2022b, *ApJ*, 941, 120, doi: [10.3847/1538-4357/aca1b4](https://doi.org/10.3847/1538-4357/aca1b4)
- Haid, S., Walch, S., Seifried, D., et al. 2018, *MNRAS*, 478, 4799, doi: [10.1093/mnras/sty1315](https://doi.org/10.1093/mnras/sty1315)
- Hennebelle, P., & Iffrig, O. 2014, *A&A*, 570, A81, doi: [10.1051/0004-6361/201423392](https://doi.org/10.1051/0004-6361/201423392)
- Hill, A. S., Joung, M. R., Mac Low, M.-M., et al. 2012, *ApJ*, 750, 104, doi: [10.1088/0004-637X/750/2/104](https://doi.org/10.1088/0004-637X/750/2/104)
- Hirai, Y., Fujii, M. S., & Saitoh, T. R. 2021, *PASJ*, 73, 1036, doi: [10.1093/pasj/psab038](https://doi.org/10.1093/pasj/psab038)
- Hislop, J. M., Naab, T., Steinwandel, U. P., et al. 2022, *MNRAS*, 509, 5938, doi: [10.1093/mnras/stab3347](https://doi.org/10.1093/mnras/stab3347)
- Hopkins, P. F. 2015, *MNRAS*, 450, 53, doi: [10.1093/mnras/stv195](https://doi.org/10.1093/mnras/stv195)
- Hopkins, P. F., & Raives, M. J. 2016, *MNRAS*, 455, 51, doi: [10.1093/mnras/stv2180](https://doi.org/10.1093/mnras/stv2180)
- Hu, C.-Y. 2019, *MNRAS*, 483, 3363, doi: [10.1093/mnras/sty3252](https://doi.org/10.1093/mnras/sty3252)
- Hu, C.-Y. 2021, *huchiayu/AstroChemistry.jl*: v0.2.2, Zenodo, doi: [10.5281/zenodo.4775808](https://doi.org/10.5281/zenodo.4775808)
- Hu, C.-Y., Naab, T., Glover, S. C. O., Walch, S., & Clark, P. C. 2017, *MNRAS*, 471, 2151, doi: [10.1093/mnras/stx1773](https://doi.org/10.1093/mnras/stx1773)
- Hu, C.-Y., Naab, T., Walch, S., Glover, S. C. O., & Clark, P. C. 2016, *MNRAS*, 458, 3528, doi: [10.1093/mnras/stw544](https://doi.org/10.1093/mnras/stw544)
- Hu, C.-Y., Schrubba, A., Sternberg, A., & van Dishoeck, E. F. 2022, *ApJ*, 931, 28, doi: [10.3847/1538-4357/ac65fd](https://doi.org/10.3847/1538-4357/ac65fd)
- Hu, C.-Y., Sternberg, A., & van Dishoeck, E. F. 2021, *ApJ*, 920, 44, doi: [10.3847/1538-4357/ac0dbd](https://doi.org/10.3847/1538-4357/ac0dbd)
- . 2023a, *ApJ*, 952, 140, doi: [10.3847/1538-4357/acdcfa](https://doi.org/10.3847/1538-4357/acdcfa)
- Hu, C.-Y., Smith, M. C., Teyssier, R., et al. 2023b, *ApJ*, 950, 132, doi: [10.3847/1538-4357/accf9e](https://doi.org/10.3847/1538-4357/accf9e)
- Iffrig, O., & Hennebelle, P. 2017, *A&A*, 604, A70, doi: [10.1051/0004-6361/201630290](https://doi.org/10.1051/0004-6361/201630290)
- Joung, M. K. R., & Mac Low, M.-M. 2006, *ApJ*, 653, 1266, doi: [10.1086/508795](https://doi.org/10.1086/508795)
- Kannan, R., Marinacci, F., Simpson, C. M., Glover, S. C. O., & Hernquist, L. 2020, *MNRAS*, 491, 2088, doi: [10.1093/mnras/stz3078](https://doi.org/10.1093/mnras/stz3078)
- Kennicutt, Robert C., J. 1998, *ApJ*, 498, 541, doi: [10.1086/305588](https://doi.org/10.1086/305588)
- Kim, C. G., & Ostriker, E. C. 2015, *ApJ*, 802, 99, doi: [10.1088/0004-637X/802/2/99](https://doi.org/10.1088/0004-637X/802/2/99)
- Kim, C.-G., & Ostriker, E. C. 2017, *ApJ*, 846, 133, doi: [10.3847/1538-4357/aa8599](https://doi.org/10.3847/1538-4357/aa8599)
- Kim, C.-G., & Ostriker, E. C. 2018, *ApJ*, 853, 173, doi: [10.3847/1538-4357/aaa5ff](https://doi.org/10.3847/1538-4357/aaa5ff)
- Kim, C.-G., Ostriker, E. C., Fielding, D. B., et al. 2020a, *ApJL*, 903, L34, doi: [10.3847/2041-8213/abc252](https://doi.org/10.3847/2041-8213/abc252)
- Kim, C.-G., Ostriker, E. C., Somerville, R. S., et al. 2020b, *ApJ*, 900, 61, doi: [10.3847/1538-4357/aba962](https://doi.org/10.3847/1538-4357/aba962)
- Kim, C.-G., Ostriker, E. C., Kim, J.-G., et al. 2024, *ApJ*, 972, 67, doi: [10.3847/1538-4357/ad59ab](https://doi.org/10.3847/1538-4357/ad59ab)
- Klessen, R. S., & Glover, S. C. O. 2016, *Saas-Fee Advanced Course*, 43, 85, doi: [10.1007/978-3-662-47890-5\\_2](https://doi.org/10.1007/978-3-662-47890-5_2)
- Kroupa, P. 2002, *Sci. (New York, N.Y.)*, 295, 82, doi: [10.1126/science.1067524](https://doi.org/10.1126/science.1067524)
- Lahén, N., Naab, T., Johansson, P. H., et al. 2019, *ApJL*, 879, L18, doi: [10.3847/2041-8213/ab2a13](https://doi.org/10.3847/2041-8213/ab2a13)
- . 2020a, *ApJ*, 904, 71, doi: [10.3847/1538-4357/abc001](https://doi.org/10.3847/1538-4357/abc001)
- . 2020b, *ApJ*, 891, 2, doi: [10.3847/1538-4357/ab7190](https://doi.org/10.3847/1538-4357/ab7190)
- Lahén, N., Naab, T., & Szécsi, D. 2024, *MNRAS*, 530, 645, doi: [10.1093/mnras/stae904](https://doi.org/10.1093/mnras/stae904)
- Lahén, N., Naab, T., Kauffmann, G., et al. 2023, *MNRAS*, 522, 3092, doi: [10.1093/mnras/stad1147](https://doi.org/10.1093/mnras/stad1147)
- Lancaster, L., Ostriker, E. C., Kim, J.-G., & Kim, C.-G. 2021a, *ApJ*, 914, 89, doi: [10.3847/1538-4357/abf8ab](https://doi.org/10.3847/1538-4357/abf8ab)
- . 2021b, *ApJ*, 914, 90, doi: [10.3847/1538-4357/abf8ac](https://doi.org/10.3847/1538-4357/abf8ac)
- Leroy, A. K., Walter, F., Brinks, E., et al. 2008, *AJ*, 136, 2782, doi: [10.1088/0004-6256/136/6/2782](https://doi.org/10.1088/0004-6256/136/6/2782)
- Leroy, A. K., Schinnerer, E., Hughes, A., et al. 2021, *ApJS*, 257, 43, doi: [10.3847/1538-4365/ac17f3](https://doi.org/10.3847/1538-4365/ac17f3)
- Liu, J., Qiu, K., & Zhang, Q. 2022, *ApJ*, 925, 30, doi: [10.3847/1538-4357/ac3911](https://doi.org/10.3847/1538-4357/ac3911)
- Madau, P., & Dickinson, M. 2014, *ARA&A*, 52, 415, doi: [10.1146/annurev-astro-081811-125615](https://doi.org/10.1146/annurev-astro-081811-125615)
- McKee, C. F., & Ostriker, E. C. 2007, *ARA&A*, 45, 565, doi: [10.1146/annurev.astro.45.051806.110602](https://doi.org/10.1146/annurev.astro.45.051806.110602)
- Moster, B. P., Naab, T., & White, S. D. M. 2018, *MNRAS*, 477, 1822, doi: [10.1093/mnras/sty655](https://doi.org/10.1093/mnras/sty655)
- Naab, T., & Ostriker, J. P. 2017, *ARA&A*, 55, 59, doi: [10.1146/annurev-astro-081913-040019](https://doi.org/10.1146/annurev-astro-081913-040019)
- Navarro, J. F., Frenk, C. S., & White, S. D. M. 1997, *ApJ*, 490, 493, doi: [10.1086/304888](https://doi.org/10.1086/304888)
- Ostriker, E. C., & Kim, C.-G. 2022, *ApJ*, 936, 137, doi: [10.3847/1538-4357/ac7de2](https://doi.org/10.3847/1538-4357/ac7de2)
- Ostriker, E. C., McKee, C. F., & Leroy, A. K. 2010, *ApJ*, 721, 975, doi: [10.1088/0004-637X/721/2/975](https://doi.org/10.1088/0004-637X/721/2/975)
- Ostriker, E. C., & Shetty, R. 2011, *ApJ*, 731, 41, doi: [10.1088/0004-637X/731/1/41](https://doi.org/10.1088/0004-637X/731/1/41)
- Padoan, P., & Nordlund, Å. 1999, *ApJ*, 526, 279, doi: [10.1086/307956](https://doi.org/10.1086/307956)

- Partmann, C., Naab, T., Lahén, N., et al. 2024, arXiv e-prints, arXiv:2409.18096, doi: [10.48550/arXiv.2409.18096](https://doi.org/10.48550/arXiv.2409.18096)
- Pattle, K., Fissel, L., Tahani, M., Liu, T., & Ntormousi, E. 2023, in *Astronomical Society of the Pacific Conference Series*, Vol. 534, *Protostars and Planets VII*, ed. S. Inutsuka, Y. Aikawa, T. Muto, K. Tomida, & M. Tamura, 193, doi: [10.48550/arXiv.2203.11179](https://doi.org/10.48550/arXiv.2203.11179)
- Powell, K. G., Roe, P. L., Linde, T. J., Gombosi, T. I., & De Zeeuw, D. L. 1999, *Journal of Computational Physics*, 154, 284, doi: [10.1006/jcph.1999.6299](https://doi.org/10.1006/jcph.1999.6299)
- Rathjen, T.-E., Naab, T., Walch, S., et al. 2023, *MNRAS*, 522, 1843, doi: [10.1093/mnras/stad1104](https://doi.org/10.1093/mnras/stad1104)
- Rathjen, T.-E., Walch, S., Naab, T., et al. 2024, arXiv e-prints, arXiv:2410.00124, doi: [10.48550/arXiv.2410.00124](https://doi.org/10.48550/arXiv.2410.00124)
- Sembach, K. R., Howk, J. C., Ryans, R. S. I., & Keenan, F. P. 2000, *ApJ*, 528, 310, doi: [10.1086/308173](https://doi.org/10.1086/308173)
- Simpson, C. M., Pakmor, R., Marinacci, F., et al. 2016, *ApJL*, 827, L29, doi: [10.3847/2041-8205/827/2/L29](https://doi.org/10.3847/2041-8205/827/2/L29)
- Smith, M. C. 2021, *MNRAS*, 502, 5417, doi: [10.1093/mnras/stab291](https://doi.org/10.1093/mnras/stab291)
- Spitzer, Lyman, J. 1942, *ApJ*, 95, 329, doi: [10.1086/144407](https://doi.org/10.1086/144407)
- Springel, V. 2005, *MNRAS*, 364, 1105, doi: [10.1111/j.1365-2966.2005.09655.x](https://doi.org/10.1111/j.1365-2966.2005.09655.x)
- Steinwandel, U. P., Bryan, G. L., Somerville, R. S., Hayward, C. C., & Burkhardt, B. 2023, *MNRAS*, 526, 1408, doi: [10.1093/mnras/stad2744](https://doi.org/10.1093/mnras/stad2744)
- Steinwandel, U. P., & Goldberg, J. A. 2023, arXiv e-prints, arXiv:2310.11495, doi: [10.48550/arXiv.2310.11495](https://doi.org/10.48550/arXiv.2310.11495)
- Steinwandel, U. P., Kim, C.-G., Bryan, G. L., et al. 2024a, *ApJ*, 960, 100, doi: [10.3847/1538-4357/ad09e1](https://doi.org/10.3847/1538-4357/ad09e1)
- Steinwandel, U. P., Moster, B. P., Naab, T., Hu, C.-Y., & Walch, S. 2020, *MNRAS*, 495, 1035, doi: [10.1093/mnras/staa821](https://doi.org/10.1093/mnras/staa821)
- Steinwandel, U. P., Rennehan, D., Orr, M. E., Fielding, D. B., & Kim, C.-G. 2024b, arXiv e-prints, arXiv:2407.14599, doi: [10.48550/arXiv.2407.14599](https://doi.org/10.48550/arXiv.2407.14599)
- Sun, J., Leroy, A. K., Ostriker, E. C., et al. 2023, *ApJL*, 945, L19, doi: [10.3847/2041-8213/acbd9c](https://doi.org/10.3847/2041-8213/acbd9c)
- Tacconi, L. J., Genzel, R., & Sternberg, A. 2020, arXiv:2003.06245, doi: [10.1146/annurev-astro-082812-141034](https://doi.org/10.1146/annurev-astro-082812-141034)
- Tricco, T. S., & Price, D. J. 2012, *Journal of Computational Physics*, 231, 7214, doi: [10.1016/j.jcp.2012.06.039](https://doi.org/10.1016/j.jcp.2012.06.039)
- Walch, S., Girichidis, P., Naab, T., et al. 2015, *MNRAS*, 454, 238, doi: [10.1093/mnras/stv1975](https://doi.org/10.1093/mnras/stv1975)
- Wong, T., Cao, Y., Luo, Y., et al. 2024, *ApJS*, 271, 35, doi: [10.3847/1538-4365/ad20c9](https://doi.org/10.3847/1538-4365/ad20c9)
- Zhang, E., Sales, L. V., Marinacci, F., et al. 2024, arXiv e-prints, arXiv:2406.10338, doi: [10.48550/arXiv.2406.10338](https://doi.org/10.48550/arXiv.2406.10338)

## APPENDIX A - FEEDBACK YIELDS

Here we present the feedback yields for our different models, and compare them to the results of [Kim et al. \(2024\)](#). In Fig. 12 we show the total, thermal, magnetic, and turbulent yields as a function of  $P_{\text{DE}}$ , computed by averaging the respective yield over the period 200-500 Myr in each simulation. For simulations in group M, we find that our total feedback yield follows a similar slope to that of [Kim et al. \(2024\)](#), but with a normalization that is higher by a factor of  $\sim 2$ . Examining the individual pressure components, we find that at low values of  $P_{\text{DE}}$ , the thermal and turbulent yield are both higher in our simulations, with the latter dominating the pressure. At higher values of  $P_{\text{DE}}$ , both the thermal and turbulent yields approach the [Kim et al. \(2024\)](#) fit, but the magnetic pressure component becomes dominant and causes the total yield to still be higher. In group H and HV, we find that the total yield is slightly higher than in group M, driven by the turbulent component. While not a large difference, it can be explained by the more effective supernovae feedback in group H due the faster gravitational collapse of molecular clouds in the absence of magnetic pressure.

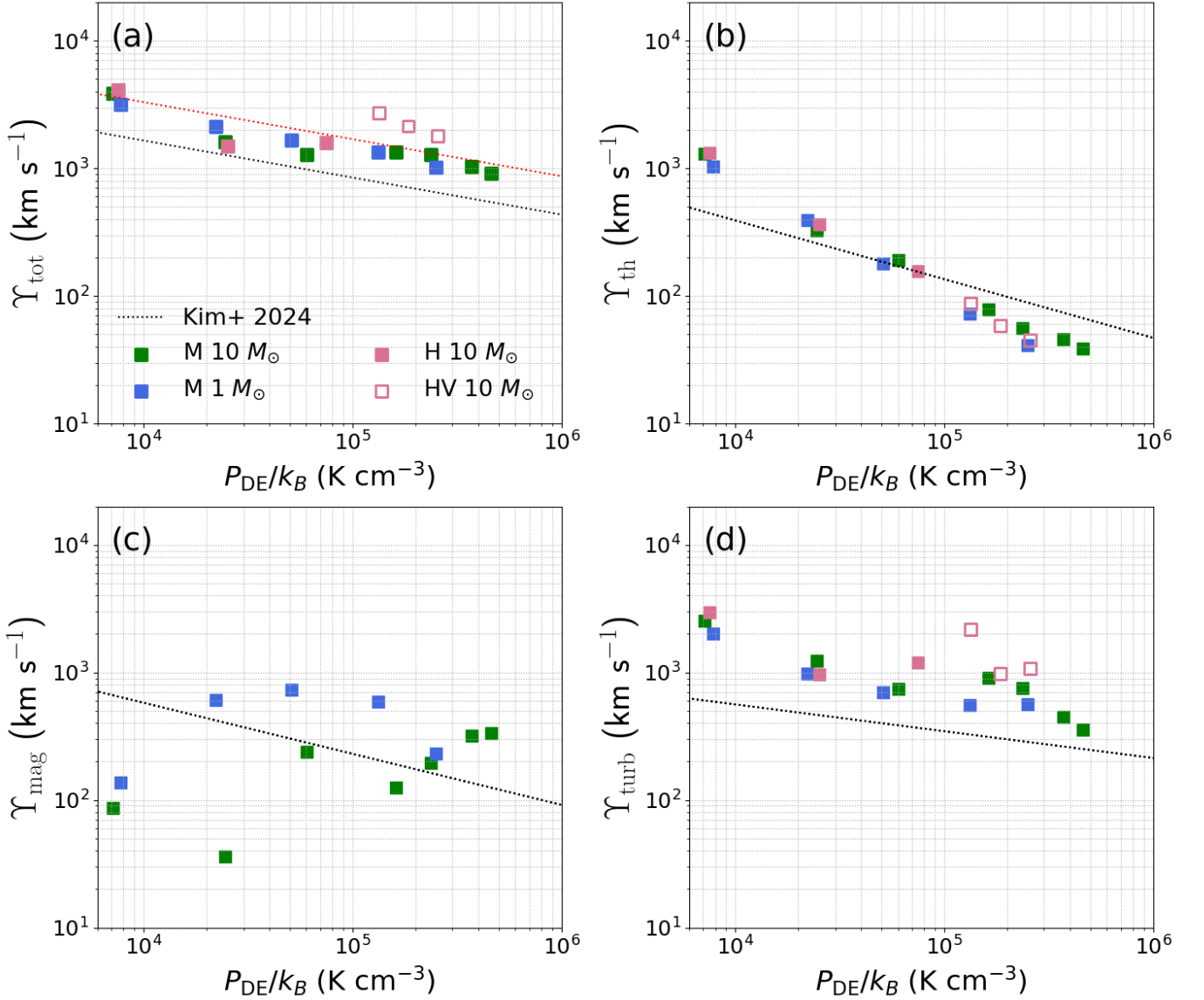


**Figure 12.** Feedback yields as a function of gas weight as estimated by  $P_{\text{DE}}$  for our different simulation groups. Dotted black lines show fits to the results of [Kim et al. \(2024\)](#) and the dotted red line shows their fit scaled up by a factor of 2, for reference.

## APPENDIX B - EVOLUTION OF THE MAGNETIC FIELD CONFIGURATION

Our analysis of the magnetic field strength requires that the magnetic field configuration and magnitude arises self-consistently from our simulations without a dependence on initial conditions. In Sec. 4 we showed that the magnetic field strength reaches a quasi-steady state. Here we show our magnetic configuration is also independent of initial conditions. Fig. 13 shows the mass-weighted average of the value of  $(B_x/B)^2$ , where  $B_x$  is the  $x$ -component of the magnetic field, and  $B$  is its magnitude. It includes simulations with a mass resolution of  $10 M_\odot$  only, with the initial magnetic field listed in the legend of each panel. While the initial value is 1 in group M by construction, it is closer to  $1/3$  for group MV, and we would expect it to decrease to or remain approximately at that value for us to determine that the initial conditions of the simulation have been erased. Indeed, Fig. 13 shows that all of the simulations in group M and HM, respectively in red and blue, reach this desired state. In fact, this holds for a number of other tests simulations where we vary the initial magnetic field. We do find, however, that if the initial magnetic field is high enough (for a given gas surface density),  $B_x$  can continue dominating for several hundred Myr, as is demonstrated in the  $B_0 = 5 \mu G$  runs for the two lowest gas surface densities. This is therefore a test that MHD galactic patch simulations should pass in order to avoid a, initial conditions-dominated magnetic field.

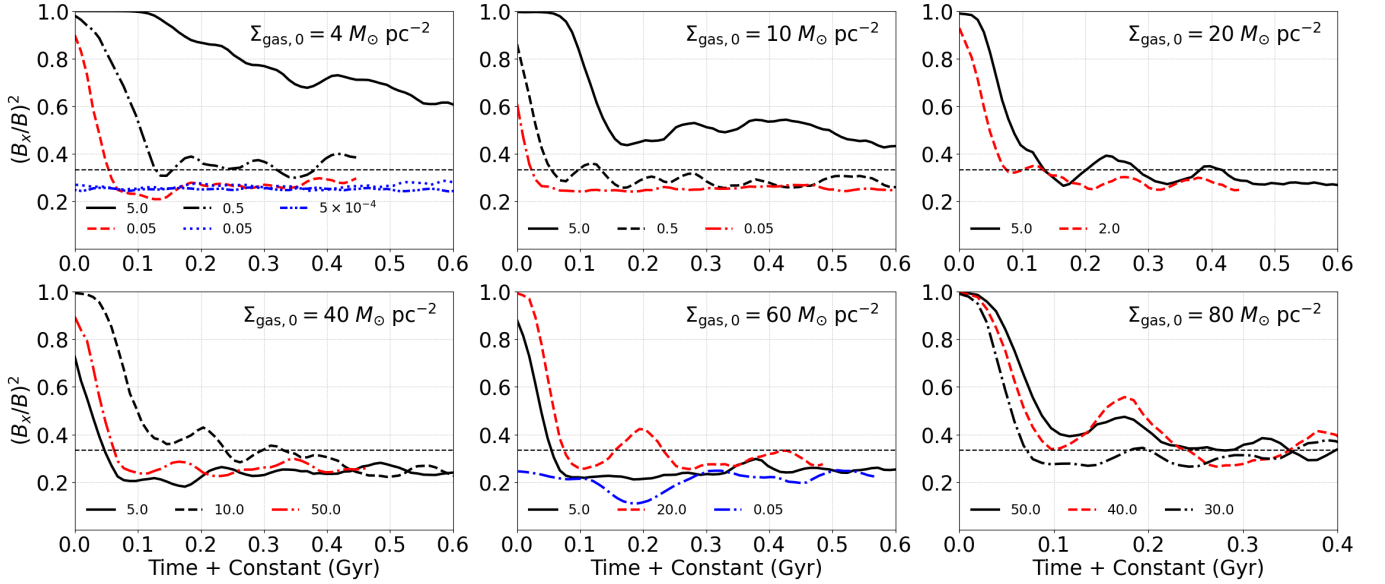


**Figure 13.** Time dependence of the relative strength of the  $x$ -component of the magnetic field, as represented by  $(B_x/B)^2$ . Each panel consists of simulations with  $\Sigma_{\text{gas},0}$  specified in its top right corner. Red lines are simulations from group M, blue line are simulations from group MV, and black lines have the setup of group M but a different value of  $B_0$ , specified in the legend. We apply a 50 Myr moving average to the results for easier visualization.